



Computational Science and Engineering (International Master's Program)

Technische Universität München

Master's Thesis

Hybrid algorithm for the Vlasov-Poisson system

Asad Ali





Computational Science and Engineering (International Master's Program)

Technische Universität München

Master's Thesis

Hybrid algorithm for the Vlasov-Poisson system

Author:

Asad Ali

1st examiner:

Univ.-Prof. Dr. Eric Sonnendrücker

2nd examiner:

Univ.-Prof. Dr. Hans-Joachim Bungartz

Assistant advisor: Dr. Stefan Possanner

Submission Date: January 30, 2018



I hereby declare that this thesis is entirely the result of my own work except where otherwise indicated. I have only used the resources given in the list of references.

January 30, 2018

Asad Ali

Acknowledgments

I would like to express my gratitude to my thesis supervisor Dr. Stefan Possanner for his participation, remarks and engagement throughout this master thesis. His guidance helped me in research, implementation and writing of this thesis. I would also like to thank all of my teachers for enabling me to achieve this milestone.

"I have no special talent. I am only passionately curious."

-Albert Einstein

Abstract

The topic of this thesis is the numerical solution of the one-dimensional Vlasov-Poisson system by means of a hybrid strategy, using the information of the fluid moments. The aim is to develop high-order coupling schemes for the kinetic-fluid hybrid system, where the kinetic part is solved with a particle-in-cell Monte-Carlo method while the fluid part is solved with a high-order finite volume scheme. The fluid moments are used to construct a control variate for the Monte-Carlo integration of the heat flux. Moreover, the Plasma density as a solution of the fluid equations can be used in the right-hand-side of Poisson's equation, leading to a new algorithm for the Vlasov-Poisson system. Test cases include the linear Landau damping initial conditions, as well as the two-stream and the bump-on-tail instabilities.

Contents

Acknowledgements	iv
Abstract	vi
I. Introduction and Background Theory	1
1. Introduction	2
1.1. Plasma physics	2
1.2. Hybrid numerical schemes	4
1.3. Organization of the thesis	5
2. Theoretical aspects	7
2.1. The Vlasov-Poisson system	7
2.1.1. Problem Statement	7
2.1.2. Derivation from Vlasov-Maxwell	7
2.1.3. Characteristics	8
2.1.4. Conservation Laws	8
2.1.5. Dispersion relation	9
2.2. Fluid Equations	11
2.2.1. Velocity moments of Vlasov	11
2.2.2. Euler Equations	13
2.2.3. Exact solution of linearized Euler equations	15
2.3. Monte Carlo simulation	17
2.3.1. Basics of probability theory	17
2.3.2. Estimators	18
II. Body: What was done for the thesis	20
3. Numerical Methods	21
3.1. The kinetic solver	21
3.1.1. Principle of a PIC solver	21
3.1.2. Monte Carlo integration	22
3.1.3. Electric field at marker positions	24
3.1.4. PIC method cycle	24
3.2. The fluid solver	24
3.2.1. Finite volume method	25
3.2.2. ENO reconstruction scheme	26
3.2.3. MUSCL scheme	26

Contents

3.2.4. Discretization in time	27
3.3. Hybrid scheme	27
III. Results and Conclusion	31
4. Simulation Results	32
4.1. PIC verification tests	32
4.1.1. Linear Landau damping	32
4.1.2. Two stream instability	33
4.1.3. Bump-on-tail instability	33
4.2. Verification of the fluid solver	33
4.2.1. Convergence of ENO reconstruction	34
4.2.2. Convergence of fluid solver	34
4.3. Hybrid tests	34
4.4. Simulation figures	35
5. Conclusion	49
Bibliography	49

Part I.

Introduction and Overview

1. Introduction

1.1. Plasma physics

Plasmas are quasi-neutral many-particle systems which are formed when the matter is heated at such a high temperature such that electrons leave their orbit around the nuclei [6]. This mixture of electrons and ions forms a new state of matter called plasma, see Figure 1.1. Plasma is the most dominant form of matter in the universe. Almost 99% of the visible universe is in the form of plasma. The examples of naturally occurring plasmas include lightning, ionosphere, plasma sphere or polar winds. The examples of artificially produced plasmas are plasma displays, inside fluorescent lamps or fusion devices.

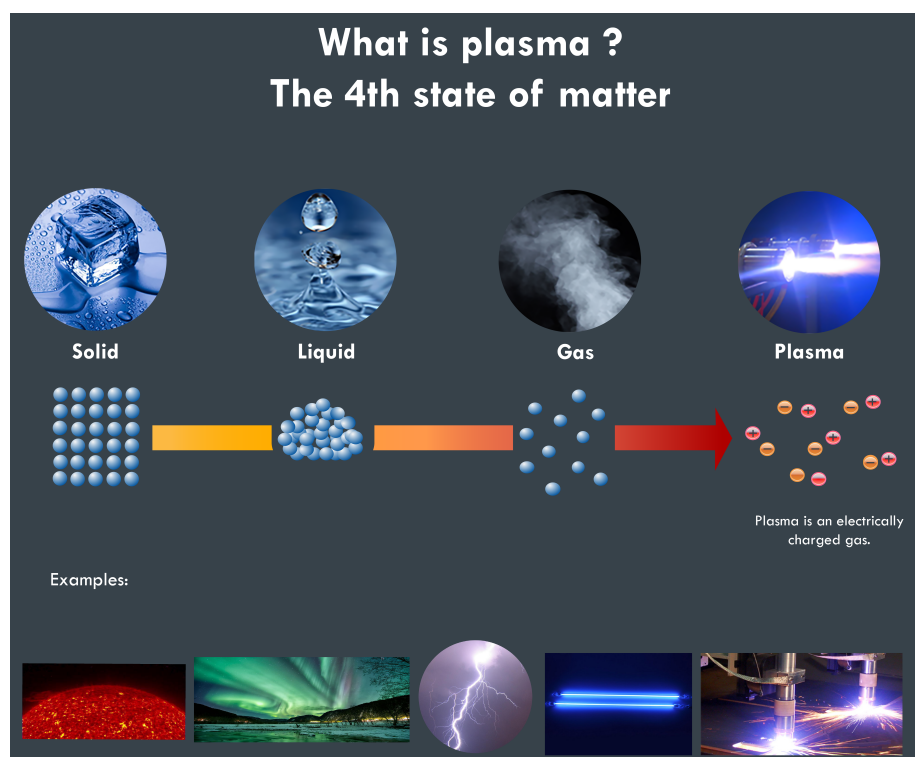


Figure 1.1.: Plasma is the fourth state of matter which is formed when matter is heated to a very high temperature such that matter is ionized. (Image was downloaded from <http://www.pyrogenesis.com/blog/infographic-plasma/>)

Aside from experimental observations in natural or laboratory plasmas, the study of plasma properties relies on theoretical and numerical analysis, based on model equations (or just "models"). Plasma models come in different complexity:

1. *Microscopic model*: each particle is described by an equation of motion.

1. Introduction

2. *Mesoscopic model*: the plasma is described by a position-velocity distribution function in phase space.

3. *Macroscopic model*: the plasma is described by its density, pressure and velocity.

The complexity and thus the content of information decreases from model 1) to model 3). The microscopic model is the hardest one to solve. Here, we are solving as many equations as the number of individual particles. This model cannot be solved even with the most advanced computational resources. On the other hand the macroscopic models (e.g MHD) are less expensive but also less accurate. Mesoscopic models are a good compromise between microscopic and macroscopic models. The Vlasov-Poisson (VP) model, which belongs to the mesoscopic models, is one such model which plays a prominent role in the study of space plasmas, galaxy formation, solar physics and controlled fusion.

Nuclear Fusion is the process by which the stars produce their energy. It is a nuclear reaction in which two or more atomic nuclei collide at a very high energy and fuse together to form a new nucleus, e.g. helium, along with excess energy, see Figure 1.2. Fusion has the potential to solve the world energy problem in the future. To harness the fusion energy on earth, plasma should be held together (confined) at very high temperatures, for long enough time to get the reaction started. In experiments the plasma is confined by the application of electric and magnetic fields, which form a "magnetic cage". This complex interaction of plasma particles with electric and magnetic field is described by the Vlasov-Maxwell system. Solution of these equations is important not only for magnetically confined fusion, but also for space physics (solar flares, solar wind) [4].

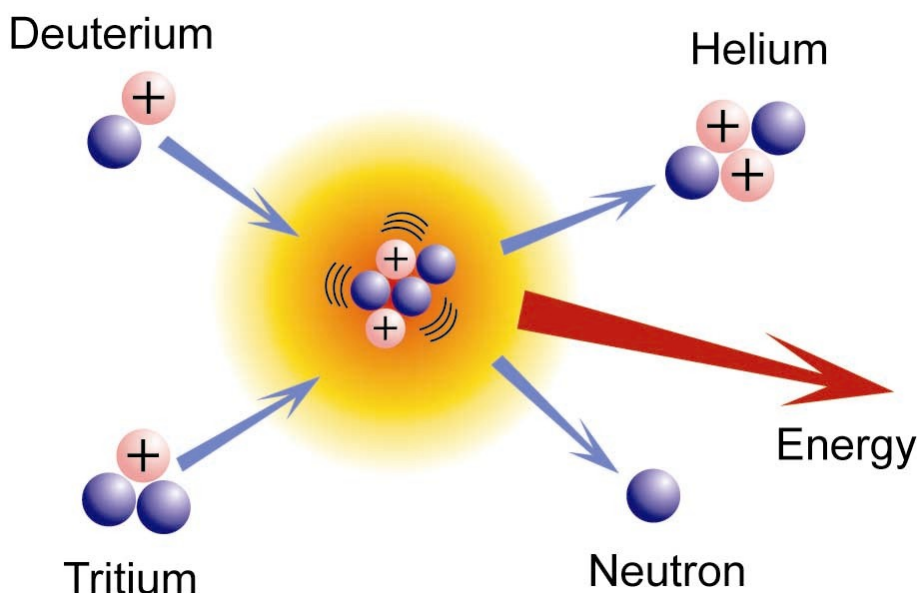


Figure 1.2.: Illustration of the Deuterium, Tritium fusion reaction. (Image was downloaded from <https://chem.libretexts.org/>)

The high dimensionality of the phase space makes the solution of Vlasov-Maxwell very costly and one often resorts to particle (PIC) methods (solution of a large number of ordinary differential equations). The efficiency and applicability of these methods rely strongly on

1. Introduction

the reduction of statistical noise in the computation of Monte-Carlo integrals. Such variance reduction can be achieved with so-called hybrid or multi-scale techniques.

Hybrid numerical schemes are a topic that is getting more and more attention in the plasma physics and applied mathematics community. Much effort is being put into the clever coupling of high-resolution kinetic solvers to coarse solvers or even to fluid solvers in order to improve efficiency. Recent developments in numerics and in high performance computing have made it possible to study the plasma models in great detail. The aim of this thesis is to explore some possibilities of variance-reduction in a PIC solver by use of the moment equations obtained from the Vlasov equation.

Let $f_s(t, \mathbf{x}, \mathbf{v})$ denote the distribution function of the species s in the plasma, where $\mathbf{x} \in \mathbb{R}^3$ stands for particle's position, and $\mathbf{v} \in \mathbb{R}^3$ for particle's velocity. Then the Vlasov equation governs the evolution of this distribution function in the phase space $\mathbb{R}^3 \times \mathbb{R}^3$. Coupled with Maxwell equations, this system forms the kinetic (mesoscopic) description of the plasma:

$$\frac{\partial f_s}{\partial t} + \mathbf{v} \cdot \frac{\partial f_s}{\partial \mathbf{x}} + \frac{q_s}{m_s} (\mathbf{E} + \mathbf{v} \times \mathbf{B}) \cdot \frac{\partial f_s}{\partial \mathbf{v}} = \sum_s Q(f_s, f'_s), \quad (1.1a)$$

$$-\frac{1}{c^2} \frac{\partial \mathbf{E}}{\partial t} + \nabla \times \mathbf{B} = \mu_0 \mathbf{J}, \quad (1.1b)$$

$$\frac{\partial \mathbf{B}}{\partial t} + \nabla \times \mathbf{E} = 0, \quad (1.1c)$$

$$\nabla \cdot \mathbf{E} = \frac{\rho}{\epsilon_0}, \quad (1.1d)$$

$$\nabla \cdot \mathbf{B} = 0. \quad (1.1e)$$

Here, q_s and m_s denote the electric charge and mass of the particles, respectively, \mathbf{E} is electric field and \mathbf{B} stands for the magnetic field. \mathbf{J} is the current density and ρ denotes the charge density given by

$$\rho = \sum_s q_s \int f_s d\mathbf{v}, \quad \mathbf{J} = \sum_s q_s \int v f_s d\mathbf{v}, \quad (1.2)$$

where, ϵ_0 denotes the permittivity of vacuum, μ_0 stands for the magnetic constant and c represents the speed of light in free space. $\sum_s Q(f_s, f'_s)$ denotes a collision operator, which models the inter- and intra-species collisions. A widely used linear collision operator is the Fokker-Planck operator.

A great deal of theoretical plasma physics concerns the study and (approximate) solution of this non-linearly coupled system of PDE's (1.1). Plasma waves can be studied by linear analysis of plane wave solutions, around a pre-defined equilibrium scale (linear stability analyses). A rich class of reduced models can be derived, among which are the VP-system, the multi-species fluid model, and magnetohydrodynamics (MHD) equations.

1.2. Hybrid numerical schemes

In many practical applications, small-scale phenomena are responsible for the overall large-scale behavior of a plasma, for example in plasma turbulence occurring in the high-confinement mode (H-mode) of a tokamak fusion plasma. The coupling of micro-scale and macro-scale

1. Introduction

dynamical processes pose considerable challenges from a theoretical and numerical point of view. The modeling of plasma turbulence (and fluid turbulence in general) is an active field of research. Recently, with the advent of supercomputers and high performance computing (HPC), theoretical efforts have been more and more supplemented by numerical experiments [7]. Numerical coupling of micro, meso, and macro scales need new concepts and schemes. Different strategies exist, among which we shall focus on the Kinetic-fluid coupling.

The main strategy is two fold: one either uses the information of the cheap fluid solution to speed-up the kinetic solver, or one integrates the kinetic information to improve the accuracy of the fluid solution. Different approaches exist for the Kinetic-fluid coupling. One such approach is proposed in [3], coupling the Boltzmann equation with a fluid system. The idea is to decompose the domain into kinetic and fluid regions and solve the respective equations in these regions. For this type of coupling the kinetic and fluid regions have to be identified beforehand, which is not possible in of the cases. To tackle this problem, another approach is proposed in [2]. The basic idea is to couple the fluid model and the kinetic model through a buffer zone in which both equations are solved. The time evolution of the buffer zones between the kinetic and the fluid regions is based on cut-off function which identifies the buffer zone on the basis of certain cut-off equilibrium indicators.

Another class of hybrid schemes is the variance reduction of the Monte-Carlo method with the help of a fluid model [5]. The basic idea is to solve the kinetic model using the Monte-Carlo method, and the fluid system using finite volumes and then use the fluid results to find a better control variate to improve the Monte-Carlo approximation. This way the Monte-Carlo approximation could be improved significantly because of reduced uncertainty in the control variate integral. We will explore some of these variance reduction strategies using the coupling of kinetic and fluid systems.

1.3. Organization of the thesis

The thesis is organized as follows:

In chapter 2 we present the one-dimensional Vlasov-Poisson (VP) system under consideration. Here, the VP system is derived from the Vlasov-Maxwell system. Then we give the properties of the VP system and also discuss the solution of the linearized VP system later used for the verification tests. The fluid system is derived in this chapter by taking the velocity moments of the Vlasov equation. The eigenvalues and the analytical solution of the linearized fluid system is also derived. Basic properties of the variables in Monte-Carlo integration are discussed in the last part.

In chapter 3 we introduce the numerical methods used to solve the VP system, as well as, the fluid and the hybrid system, respectively. To solve the VP system, the particle-in-cell method is used with the thermal equilibrium distribution (Maxwellian) as control variate. The particle-mesh coupling is done by smoothing the particle distribution with splines of third degree. For the fluid system we use the finite volume method. For higher order reconstruction, the essentially-non-oscillatory (ENO) scheme is applied. We also present the hybrid system here, and develop the algorithm for the integration of the coupled VP and fluid systems. The main point here is to compute the heat flux as a Monte-Carlo integral with control variate.

In chapter 4 we show the simulation results. For the VP system the results of Landau

1. Introduction

damping, two stream instability and bump on tail instability tests are given. For the fluid system, convergence of the ENO reconstruction is demonstrated. The effect of different Runge-Kutta methods used for time integration on the convergence is also discussed. For the hybrid system we present a Monte-Carlo convergence result.

2. Theoretical aspects

2.1. The Vlasov-Poisson system

The Vlasov-Poisson (VP) system is of fundamental importance in plasma physics, as it describes the reaction of a plasma to local disturbances of the quasi-neutrality condition. The (non-linear) interplay between charge separation in the plasma and the ensuing electric field leads to so called "electrostatic waves", e.g. Langmuir waves, that are absent in neutral gases. VP also allows to capture non-equilibrium effects, i.e. when the plasma is far from thermal equilibrium. A famous example is the linear and non-linear Landau damping, describing a transfer of energy from the electric field to the plasma, leading to filamentation in the velocity space distribution. Other interesting test cases include the two-stream instability and the bump on tail instability. In this section we present the VP-model as studied in this thesis, as well as some of its mathematical properties.

2.1.1. Problem Statement

Vlasov-Poisson describes the interaction of particles via an electrostatic mean field. The VP system we consider reads

$$\begin{cases} \frac{\partial f}{\partial t} + v \frac{\partial f}{\partial x} - E \frac{\partial f}{\partial v} = 0, \\ -\frac{\partial^2 \phi}{\partial x^2} = 1 - \int_{\mathbb{R}} f \, dv, \quad E = -\frac{\partial \phi}{\partial x}, \\ f(0, x, v) = f_0(x, v). \end{cases} \quad (2.1)$$

Here, $f = f(t, x, v)$ describes the electron distribution at point $(t, x, v) \in [0, T] \times \Omega$, with $\Omega = [0, L] \times \mathbb{R}$ called the phase-space. E is the self consistent electric field and ϕ is the scalar potential. We assume periodic boundary conditions in x and $\lim_{v \rightarrow \pm\infty} f(t, x, v) = 0$ for the velocity. In numerical experiments we will truncate the velocity space, i.e. we will replace \mathbb{R} by $[-L_v, L_v]$ with L_v sufficiently large such that $f(t, x, v) \approx 0$ for $|v| > L_v$.

2.1.2. Derivation from Vlasov-Maxwell

The Vlasov-Maxwell system is given in (1.1). We reduce the model to two species, namely ions and electrons. Ions are immobile with constant density $n_i = 1$. We set $q_e = m_e = 1$. In the absence of a magnetic field, $\mathbf{B} = 0$, equation (1.1c) becomes

$$\nabla \times \mathbf{E} = 0.$$

Then, because $\nabla \times \nabla \phi = 0$, for some scalar function ϕ we can write

$$\mathbf{E} = -\nabla \phi. \quad (2.2)$$

2. Theoretical aspects

Inserting (2.2) into (1.1d) and setting $\rho = n_i - n_e$ with $n_i = 1, n_e = \int f dv$, gives the Poisson equation

$$-\Delta\phi = 1 - \int_{\mathbb{R}} f dv.$$

Inserting (2.2) into (1.1b), using the identity $\epsilon_0\mu_0 = \frac{1}{c^2}$, and then taking the divergence of equation (1.1b) gives

$$\partial_t\rho + \partial_x\mathbf{J} = 0$$

which is nothing else than conservation of charge and thus redundant. Hence we have obtained the three dimensional VP system, which on reducing to 1D gives (2.1).

2.1.3. Characteristics

The Vlasov equation in (2.1) is an advection equation and, therefore f remains constant along the "characteristics" $(\mathcal{X}(t), \mathcal{V}(t))$, solution of the following system of ordinary differential equations:

$$\begin{cases} \frac{d\mathcal{X}(t)}{dt} = \mathcal{V}(t), & \mathcal{X}(t=s) = x, \\ \frac{d\mathcal{V}(t)}{dt} = -E(t, \mathcal{X}(t)), & \mathcal{V}(t=s) = v. \end{cases} \quad (2.3)$$

It is easy to see that any solution of the Vlasov equation (2.1) is constant along a solution of (2.3), because

$$\begin{aligned} \frac{d}{dt}f(t, \mathcal{X}(t), \mathcal{V}(t)) &= \partial_t f(t, \mathcal{X}(t), \mathcal{V}(t)) + \partial_x f(t, \mathcal{X}(t), \mathcal{V}(t)) \frac{\mathcal{X}(t)}{dt} + \partial_v f(t, \mathcal{X}(t), \mathcal{V}(t)) \frac{\mathcal{V}(t)}{dt}, \\ &= [\partial_t f + v \partial_x f - E \partial_v f](t, \mathcal{X}(t), \mathcal{V}(t)) = 0, \end{aligned}$$

since f satisfies the Vlasov equation. Therefore,

$$f(t, \mathcal{X}(t), \mathcal{V}(t)) = f(0, \mathcal{X}(0), \mathcal{V}(0)), \quad (2.4)$$

which is at the heart of the particle-in-cell algorithm.

2.1.4. Conservation Laws

The Vlasov-Poisson system has certain conservation properties which can be used to test the quality of a numerical scheme. Ideally, a scheme should conserve all these properties on the discrete level. The important conservation laws of the Vlasov-Poisson system are:

1) Maximum principle,

$$0 \leq f(t, x, v) \leq \max_{(x,v)}(f_0(x, v)), \quad (2.5)$$

which can easily be verified by the fact that Vlasov equation is an advection equation by nature, therefore f remains constant along the characteristics.

2) Conservation of L^p norms, where $1 \leq p \leq \infty$,

$$\frac{d}{dt} \left(\int |f(t, x, v)|^p dx dv \right) = 0, \quad (2.6)$$

2. Theoretical aspects

which can be proved by multiplying the Vlasov equation by f^{p-1} and integrating over whole phase-space.

3) Conservation of momentum,

$$\frac{d}{dt} \int v f dx dv = \frac{d}{dt} \int n u dx = 0, \quad (2.7)$$

which can be proved by multiplying the Vlasov equation by v and integrating over the whole phase-space.

4) Conservation of energy,

$$\frac{d}{dt} \left[\frac{1}{2} \int v^2 f dx dv + \frac{1}{2} \int E^2 dx \right] = 0, \quad (2.8)$$

which can be proved by multiplying the Vlasov equation by v^2 and integrating over the whole phase-space.

2.1.5. Dispersion relation

Dispersion relations describe the reaction of a system to small perturbations in the form of plane waves. The dispersion relation of Vlasov-Poisson can be found by linearizing the problem around some equilibrium, for example a Maxwellian $f^0 = f^0(v)$ (thermal equilibrium) by introducing: $f(t, x, v) = f^0(v) + \epsilon f^1(t, x, v)$ and $E(t, x) = \epsilon E^1(t, x)$ into the Vlasov-Poisson system. We assume the equilibrium electric field to be zero, $E^0(x) = 0$. By using that $\partial_t f^0 = \partial_x f^0 = 0$, $\int f^0 dv = 1$ and by neglecting the ϵ^2 -terms, one obtains the linearized system of the form

$$\frac{\partial f^1}{\partial t} + v \frac{\partial f^1}{\partial x} - E^1 \frac{\partial f^0}{\partial v} = 0, \quad (2.9)$$

$$\frac{\partial E^1}{\partial x} = - \int_{\mathbb{R}} f^1(t, x, v) dv, \quad (2.10)$$

with initial condition $f^1(0, x, v) = f_0^1(x, v)$. System (2.9)-(2.10) can be solved analytically. For this we apply the L-periodic Fourier transform to the equations by multiplying the equations (2.9) and (2.10) by e^{-ikx} and integrating from 0 to L ,

$$\frac{\partial \hat{f}(t, k, v)}{\partial t} + ikv \hat{f}(t, k, v) - \hat{E}(t, k) \frac{\partial f^0}{\partial v} = 0, \quad (2.11)$$

$$ik \hat{E}(t, k) = - \int_{-\infty}^{\infty} \hat{f}(t, k, v) dv, \quad (2.12)$$

where

$$\hat{f}(t, k, v) := \int_0^L f^1(t, x, v) e^{-ikx} dx, \quad \hat{E}(t, k) := \int_0^L E^1(t, x) e^{-ikx} dx$$

is the Fourier representation of f^1 and E^1 respectively. The second term in (2.11) has been obtained via integration by parts and in the third term we used that f^0 does not depend on x . We now apply the Laplace transform, defined by

$$\tilde{f}(\omega) = \int_0^{\infty} \hat{f}(t) e^{-i\omega t} dt, \quad \tilde{E}(\omega) = \int_0^{\infty} \hat{E}(t) e^{-i\omega t} dt, \quad \operatorname{Im}(\omega) > \omega_0 \in \mathbb{R},$$

2. Theoretical aspects

by multiplying the equation by $e^{-i\omega t}$ and integrating in time from 0 to ∞ to obtain

$$(-i\omega + ikv)\tilde{f}(\omega, k, v) - \tilde{E}(\omega, k) \frac{df^0}{dv} = \hat{f}_0(k, v), \quad (2.13)$$

$$\tilde{E}(\omega, k) = \frac{i}{k} \int_{-\infty}^{\infty} \tilde{f}(\omega, k, v) dv. \quad (2.14)$$

Plugging \tilde{f} from (2.13) into (2.14) leads to an expression of the electric field in Laplace-Fourier space:

$$\tilde{E}(\omega, k) = \frac{N(\omega, k)}{D(\omega, k)},$$

where

$$D(\omega, k) = 1 - \frac{1}{k^2} \int_{-\infty}^{\infty} \frac{\frac{df^0}{dv}}{v - \frac{\omega}{k}} dv, \quad (2.15)$$

$$N(\omega, k) = \frac{1}{k^2} \int_{-\infty}^{\infty} \frac{\hat{f}_0(k, v)}{v - \frac{\omega}{k}} dv.$$

Here, D is called the dielectric function. An analytical solution of E in t - k space is obtained via inverse Laplace transform, see [6]. The "normal modes" for given k are the modes of \tilde{E} at $D(\omega, k) = 0$. Normal modes with $Im(\omega) < 0$ are damped modes, whereas $Im(\omega) > 0$ indicates a growing mode. For fixed k , the expression $D(\omega, k) = 0$ can be solved numerically for example by the Newton method. For linear Landau damping, i.e. with $f^0(v) = \frac{1}{\sqrt{2\pi}} e^{-\frac{v^2}{2}}$ and initial condition $f_0 = (1 + \epsilon \cos(x))f^0(v)$, the analytical expression for E becomes,

$$E(t, x) \approx \frac{2\epsilon}{k} r e^{\omega_i t} \cos(\omega_r t - \pi - \phi) \sin(kx), \quad (2.16)$$

where the normal modes $\omega = \omega_r + i\omega_i$, the phase ϕ and the amplitude r are given in Table 2.1.

Table 2.1.: Coefficients for the analytical solution of electric field given in (2.16), for linear Landau damping.

k	ω_r	ω_i	r	ϕ
0.5	1.4156	-0.1533	0.3677	0.5362
0.4	1.2850	-0.0661	0.4247	0.3358
0.3	1.1598	-0.0126	0.6368	0.1143
0.2	1.0640	-5.510×10^{-5}	1.1297	0.0013

The schemes we shall develop can be verified by comparing the simulation results with analytic solutions for the electric field (2.16), and with growth and damping rates of the normal modes given in Table 2.1. Similarly for the two stream instability, the analytical growth rate is found to be $e^{\omega_i t}$ with the coefficient given in table 2.2. For bump on tail instability, the growth rate for the $v_b = 4.5$, $k = 0.3$ is given by $e^{0.198t}$.

Table 2.2.: Coefficients for analytical growth rate for the two-stream instability.

v_0	ω_i
1.3	0.0011
2.4	0.2258
3.0	0.2845

2.2. Fluid Equations

In the most general setting given in (1.1a), the Vlasov equation is a six dimensional problem (seven if one includes time), which gives the detailed velocity distribution of the particles at each point, making it computationally very expensive. To reduce the complexities, one can model the plasma by fluid equations which give the information about some macroscopic quantities. The underlying assumption for such models is that due to collisions, the system is close to thermodynamic equilibrium at all times. The fluid model is a three-dimensional model, hence computationally less expensive. We shall discuss in what follows the fluid equations corresponding to our one-dimensional VP system (2.1). The generalization to three dimensions is straight forward.

2.2.1. Velocity moments of Vlasov

Fluid equations can be derived from the Vlasov equation in (2.1) by taking velocity moments and using the following definitions:

$$n(t, x) := \int_{\mathbb{R}} f(t, x, v) dv, \quad (2.17a)$$

$$n(t, x) u(t, x) := \int_{\mathbb{R}} v f(t, x, v) dv, \quad (2.17b)$$

$$w(t, x) := \frac{1}{2} \int_{\mathbb{R}} v^2 f(t, x, v) dv, \quad (2.17c)$$

$$p(t, x) := \int_{\mathbb{R}} f(v - u)^2 dv = \int_{\mathbb{R}} f v^2 dv - n u^2. \quad (2.17d)$$

Here, n defines the density, u the plasma mean velocity, w energy of the plasma and p the pressure. In the definition of the pressure we implicitly assumed the electrons to be a monoatomic, ideal gas in one dimension. Then taking the zeroth moment of the Vlasov equation (2.1) gives:

$$\int_{\mathbb{R}} \partial_t f dv + \int_{\mathbb{R}} v \partial_x f dv - \int_{\mathbb{R}} E \partial_v f dv = 0. \quad (2.18)$$

Using that the last term vanishes due to the decay condition on f ,

$$\int_{\mathbb{R}} E \partial_v f dv = E f(v)|_{-\infty}^{\infty} = E (f(\infty) - f(-\infty)) = 0, \quad (2.19)$$

2. Theoretical aspects

and inserting the definitions (2.17a) and (2.17b), one obtains

$$\partial_t n + \partial_x(n u) = 0, \quad (2.20)$$

which is the conservation of mass equation. For the momentum equation, multiplying the Vlasov equation with v and integrating yields

$$\partial_t \int_{\mathbb{R}} v f dv + \partial_x \int_{\mathbb{R}} v^2 f dv - E \int_{\mathbb{R}} v \partial_v f dv = 0. \quad (2.21)$$

Since

$$E \int_{\mathbb{R}} v \partial_v f dv = E \left(v f \Big|_{-\infty}^{\infty} - \int_{\mathbb{R}} f \partial_v v dv \right) = -nE, \quad (2.22)$$

by using (2.17) equation (2.21) becomes:

$$\partial_t(n u) + \partial_x(n u^2 + p) = -nE, \quad (2.23)$$

which is the conservation of momentum equation. For the energy equation we multiply the Vlasov equation by v^2 and integrate to obtain

$$\partial_t \int_{\mathbb{R}} v^2 f dv + \partial_x \int_{\mathbb{R}} v^3 f dv - E \int_{\mathbb{R}} v^2 \partial_v f dv = 0. \quad (2.24)$$

At this point we define the *heat flux* q as

$$q(t, x) := \frac{1}{2} \int_{\mathbb{R}} (v - u(t, x))^3 f(t, x, v) dv. \quad (2.25)$$

We make the following observation:

$$\begin{aligned} q &= \frac{1}{2} \left[\int_{\mathbb{R}} (v^3 - u^3 - 3v^2u + 3vu^2) f dv \right] \\ &= \frac{1}{2} \left[\int_{\mathbb{R}} v^3 f dv - u^3 \int_{\mathbb{R}} f dv - 3u \int_{\mathbb{R}} v^2 f dv + 3u^2 \int_{\mathbb{R}} v f dv \right] \\ &= \frac{1}{2} \left[\int_{\mathbb{R}} v^3 f dv - u^3 n - 6u w + 3u^2 n u \right] \\ &= \frac{1}{2} \int_{\mathbb{R}} v^3 f dv - u(6w - 2n u^2). \end{aligned}$$

Hence,

$$\int_{\mathbb{R}} v^3 f dv = 2q + 2u(3w - n u^2). \quad (2.26)$$

Moreover,

$$E \int_{\mathbb{R}} v^2 \partial_v f dv = E \left(v^2 f \Big|_{-\infty}^{\infty} - \int_{\mathbb{R}} f \partial_v v^2 dv \right) = -2nuE. \quad (2.27)$$

Using (2.26) and (2.27), equation (2.24) becomes:

$$\partial_t w + \partial_x [u(3w - n u^2)] + \partial_x q = -nuE. \quad (2.28)$$

2. Theoretical aspects

Using $w = \frac{1}{2}p + \frac{1}{2}nu^2$ this can also be written as:

$$\partial_t w + \partial_x [u(w + p)] + \partial_x q = -nuE, \quad (2.29)$$

which is the conservation of energy equation. To summarize, the three lowest velocity moments of the Vlasov equation in (2.1) read

$$\left\{ \begin{array}{l} \partial_t n + \partial_x (n u) = 0, \\ \partial_t (n u) + \partial_x (n u^2 + p) = -nE, \\ \partial_t w + \partial_x (w u + np) + \partial_x q = -nuE. \end{array} \right. \quad (2.30)$$

Remark that this system is not closed, because the heat flux q still depends on the full distribution function f . An efficient numerical computation of q is one of the topics of this work.

2.2.2. Euler Equations

Setting $E = 0$ and $q = 0$ in (2.30), the velocity moments of the Vlasov equations reduce to the well-known Euler equations,

$$\partial_t n + \partial_x (n u) = 0, \quad (2.31a)$$

$$\partial_t (n u) + \partial_x (n u^2 + p) = 0, \quad (2.31b)$$

$$\partial_t w + \partial_x (w u + np) = 0. \quad (2.31c)$$

This system of equations, in conservative form, becomes

$$\partial_t Z + \partial_x F = 0, \quad (2.32)$$

where

$$Z = \begin{pmatrix} n \\ nu \\ w \end{pmatrix}, \quad F = \begin{pmatrix} nu \\ nu^2 + p \\ wu + pu \end{pmatrix}. \quad (2.33)$$

Here, F is called the (exact) *flux function*. This flux function will later be approximated by the Lax-Friedrich flux.

We derive the eigenvalues of the Euler system by starting from the conservative form of the Euler equations (2.32). By chain rule one obtains

$$\partial_t Z + A \partial_x Z = 0, \quad (2.34)$$

where $A := \frac{\partial F}{\partial Z} = \left(\frac{\partial F_i}{\partial Z_j} \right)_{i,j}$ is the Jacobian matrix. Using the identity $w = \frac{1}{2}p + \frac{1}{2}nu^2$, system (2.34) can be represented in the variables n , u and p . By making the variable changes, the mass equation becomes:

$$\partial_t n + u \partial_x n + n \partial_x u = 0. \quad (2.35)$$

2. Theoretical aspects

Similarly the momentum equation becomes

$$\begin{aligned}\partial_t(n u) + \partial_x(n u^2 + p) &= 0, \\ u\partial_t n + n\partial_t u + n\partial_x u^2 + u^2\partial_x n + \partial_x p &= 0, \\ u(-\partial_x(n u)) + n\partial_t u + 2nu\partial_x u + u^2\partial_x n + \partial_x p &= 0, \\ -nu\partial_x u - u^2\partial_x n + n\partial_t u + 2nu\partial_x u + u^2\partial_x n + \partial_x p &= 0,\end{aligned}$$

which yields

$$\partial_t u + u\partial_x u + \frac{1}{n}\partial_x p = 0. \quad (2.36)$$

And finally the energy equation becomes

$$\begin{aligned}\partial_t w + \partial_x(w u + up) &= 0, \\ \partial_t(n u^2 + p) + (nu^2 + p)\partial_x u + u\partial_x(nu^2 + p) + 2\partial_x(up) &= 0, \\ u\partial_t(n u) + nu\partial_t u + \partial_t p + (nu^2 + p)\partial_x u + u\partial_x(nu^2 + p) + 2\partial_x(up) &= 0,\end{aligned}$$

Here, the first and the fifth term cancel, because of equation (2.31b). Moreover, using equation (2.36) one obtains

$$-nu(u\partial_x u + \frac{1}{n}\partial_x p) + \partial_t p + (nu^2 + p)\partial_x u + 2u\partial_x p + 2p\partial_x u = 0.$$

Finally, this yields

$$\partial_t p + u\partial_x p + 3p\partial_x u = 0. \quad (2.37)$$

The system of Euler equations, in terms of the non-conservative (n, u, p) variables, reads

$$\begin{cases} \partial_t n + u\partial_x n + n\partial_x u = 0, \\ \partial_t u + u\partial_x u + \frac{1}{n}\partial_x p = 0, \\ \partial_t p + u\partial_x p + 3p\partial_x u = 0. \end{cases} \quad (2.38)$$

Introducing the new vector of moments $Z^* = \begin{pmatrix} n \\ u \\ p \end{pmatrix}$ and the matrix A^* given by:

$$A^* = \begin{bmatrix} u & n & 0 \\ 0 & u & 1/n \\ 0 & 3p & u \end{bmatrix},$$

we write this system as

$$\partial_t Z^* + A^* \partial_x Z^* = 0. \quad (2.39)$$

The eigenvalues $(\lambda_i)_i$ of A^* can be found by solving the characteristic equations $\det|A^* - \lambda I| = 0$, which reads

$$(u - \lambda) [(u - \lambda)^2 - 3p/n] = 0. \quad (2.40)$$

The roots of this equation read

$$\lambda_{1,2,3} = (u, u + \sqrt{3p/n}, u - \sqrt{3p/n}). \quad (2.41)$$

They represent the characteristic wave speeds of the Euler equations.

2.2.3. Exact solution of linearized Euler equations

An exact solution of the system (2.31) can be found by linearization of the equations around a homogeneous equilibrium:

$$n_0 = \text{const.}, \quad u_0 = \text{const.}, \quad p_0 = \text{const.} \quad (2.42)$$

Assuming a solution of the form

$$n = n_0 + \epsilon n_1, \quad (2.43a)$$

$$u = u_0 + \epsilon u_1, \quad (2.43b)$$

$$p = p_0 + \epsilon p_1, \quad (2.43c)$$

where $\epsilon \ll 1$ is a small parameter, inserting it into the system (2.38), and neglecting the 2nd order terms in ϵ one obtains

$$\partial_t \begin{pmatrix} n^1 \\ u^1 \\ p^1 \end{pmatrix} + A_0^* \partial_x \begin{pmatrix} n^1 \\ u^1 \\ p^1 \end{pmatrix} = 0, \quad (2.44)$$

where the Jacobian matrix reads

$$A_0^* = \begin{bmatrix} u_0 & n_0 & 0 \\ 0 & u_0 & 1/n_0 \\ 0 & 3p_0 & u_0 \end{bmatrix}.$$

According to (2.41) the eigenvalues are

$$\lambda_{1,2,3} = (u_0 - c, u_0, u_0 + c), \quad (2.45)$$

where $c = \sqrt{3p_0/n_0}$. Our aim is now to diagonalize the system (2.44). Solving for the eigenspaces corresponding to the respective eigenvalues yields

$$E_1 = \ker(A - (u_0 - c)I) = \ker \begin{bmatrix} c & n_0 & 0 \\ 0 & c & 1/n_0 \\ 0 & 3p_0 & c \end{bmatrix} = \langle (1, -c/n_0, c^2)^T \rangle, \quad (2.46)$$

$$E_2 = \ker(A - u_0 I) = \ker \begin{bmatrix} 0 & n_0 & 0 \\ 0 & 0 & 1/n_0 \\ 0 & 3p_0 & 0 \end{bmatrix} = \langle (1, 0, 0)^T \rangle, \quad (2.47)$$

$$E_3 = \ker(A - (u_0 + c)I) = \ker \begin{bmatrix} -c & n_0 & 0 \\ 0 & -c & 1/n_0 \\ 0 & 3p_0 & -c \end{bmatrix} = \langle (1, c/n_0, c^2)^T \rangle. \quad (2.48)$$

So the eigenvector matrix S becomes

$$S = \begin{bmatrix} 1 & 1 & 1 \\ -c/n_0 & 0 & c/n_0 \\ c^2 & 0 & c^2 \end{bmatrix}, \quad (2.49)$$

2. Theoretical aspects

and the inverse of S is calculated to be

$$S^{-1} = \begin{bmatrix} 0 & -n_0/2c & 1/2c^2 \\ 1 & 0 & -1/c^2 \\ 0 & n_0/2c & 1/2c^2 \end{bmatrix}. \quad (2.50)$$

Since the inverse of A_0^* exists it can be diagonalize as:

$$A_0^* = SDS^{-1}, \quad (2.51)$$

where $D = \text{diag}(u_0 - c, u_0, u_0 + c)$ is the diagonal matrix with the eigenvalues on the diagonal. Then equation (2.39) becomes:

$$\partial_t Z_1 + SDS^{-1} \partial_x Z_1 = 0, \quad (2.52)$$

where $Z_1 = \begin{pmatrix} n_1 \\ u_1 \\ p_1 \end{pmatrix}$. Multiplying (2.52) by S^{-1} from left gives

$$S^{-1} \partial_t Z_1 + S^{-1} SDS^{-1} \partial_x Z_1 = 0, \quad (2.53)$$

and since S is constant,

$$\partial_t S^{-1} Z_1 + D \partial_x S^{-1} Z_1 = 0. \quad (2.54)$$

The system (2.54) is a set of decoupled constant coefficient advection equations for the unknowns $V = S^{-1} Z_1$:

$$\partial_t V_1 + (u_0 - c) \partial_x V_1 = 0, \quad (2.55a)$$

$$\partial_t V_2 + u_0 \partial_x V_2 = 0, \quad (2.55b)$$

$$\partial_t V_3 + (u_0 + c) \partial_x V_3 = 0. \quad (2.55c)$$

Supplimented with the initial conditions

$$V_1(0, x) = V_{1,0}(x), \quad V_2(0, x) = V_{2,0}(x), \quad V_3(0, x) = V_{3,0}(x),$$

the solution of the system 2.55 is given by

$$V_1(t, x) = V_{1,0}(x - (u_0 - c)t), \quad (2.57a)$$

$$V_2(t, x) = V_{2,0}(x - u_0 t), \quad (2.57b)$$

$$V_3(t, x) = V_{3,0}(x - (u_0 + c)t). \quad (2.57c)$$

Finally, the solution Z_1 can be found by $Z_1 = SV$,

$$n_1(t, x) = V_{1,0}(x - (u_0 - c)t) + V_{2,0}(x - u_0 t) + V_{3,0}(x - (u_0 + c)t), \quad (2.58a)$$

$$u_1(t, x) = (-c/n_0) V_{1,0}(x - (u_0 - c)t) + (c/n_0) V_{3,0}(x - (u_0 + c)t), \quad (2.58b)$$

$$p_1(t, x) = c^2 V_{1,0}(x - (u_0 - c)t) + c^2 V_{3,0}(x - (u_0 + c)t). \quad (2.58c)$$

2. Theoretical aspects

Setting $t = 0$, the initial conditions for Z_1 read

$$n_{1,0}(x) = n_1(0, x) = V_{1,0}(x) + V_{2,0}(x) + V_{3,0}(x), \quad (2.59a)$$

$$u_{1,0}(x) = u_1(0, x) = (-c/n_0) V_{1,0}(x) + (c/n_0) V_{3,0}(x), \quad (2.59b)$$

$$p_{1,0}(x) = p_1(0, x) = c^2 V_{1,0}(x) + c^2 V_{3,0}(x). \quad (2.59c)$$

We deduce that an initial condition with $u_{1,0} = p_{1,0} = 0$ leads to pure advection of $n_{1,0}$ with velocity u_0 .

2.3. Monte Carlo simulation

The basic idea of Monte Carlo (MC) simulation is to use concepts from probability theory to evaluate integrals. An integral is viewed as the expected value of a random variable distributed according to a certain probability law, which is then approximated by a large number of random events. In the context of plasma physics MC simulations are called particle-in-cell (PIC) methods, they are a popular tool for solving the Vlasov-Maxwell or the Vlasov-Poisson equations, in which the velocity moments of the distribution function are interpreted as MC integrals [1]. In this section we introduce the basic notions needed in MC simulations.

2.3.1. Basics of probability theory

The proper mathematical framework for probability theory starts with the construction of a probability space as a measurable set using σ -algebras. We refrain from using these abstract objects and consider only probabilities in \mathbb{R}^n .

The main objects we consider are *random variables*. A random variable will be denoted with capital letters; it can be viewed as a pair $\mathbf{X} = (\mathbb{R}^n, g)$, where $g : \mathbb{R}^n \rightarrow \mathbb{R}_+$ is a positive function called the *probability distribution* (PDF) of \mathbf{X} . The PDF is normalized

$$\int_{\mathbb{R}^n} g(\mathbf{x}) d^n \mathbf{x} = 1, \quad (2.60)$$

and one says \mathbf{X} is distributed according to g . A point $\mathbf{x} \in \mathbb{R}^n$ is called a *sample point* and open subsets $A \subset \mathbb{R}^n$ are called *events*. The probability $P_{\mathbf{X}}(A)$ of an event A to occur is defined by

$$P_{\mathbf{X}}(A) = P(\mathbf{X} \in A) := \int_A g(\mathbf{x}) d^n \mathbf{x}. \quad (2.61)$$

Clearly, one has $P_{\mathbf{X}}(\mathbb{R}^n) = 1$ due to (2.60). To each random variable one can associate its *expected value* $\mathbb{E}(\mathbf{X})$, defined by

$$\mathbb{E}(\mathbf{X}) := \int_{\mathbb{R}^n} \mathbf{x} g(\mathbf{x}) d^n \mathbf{x}, \quad (2.62)$$

provided the integral exists (we shall assume that all integrals we write in the following exist). Moreover, for (possibly vector-valued) functions $h : \mathbb{R}^n \rightarrow \mathbb{R}^d$ with $d \geq 1$ one has

$$\mathbb{E}(h(\mathbf{X})) = \int_{\mathbb{R}^n} h(\mathbf{x}) g(\mathbf{x}) d^n \mathbf{x}. \quad (2.63)$$

2. Theoretical aspects

Other important parameters of a random variable \mathbf{X} are its *variance* $\mathbb{V}(\mathbf{X})$ and its *standard deviation* $\sigma(\mathbf{X})$, defined by

$$\mathbb{V}(\mathbf{X}) := \mathbb{E}(|\mathbf{X} - \mathbb{E}(\mathbf{X})|^2), \quad (2.64)$$

$$\sigma(\mathbf{X}) := \sqrt{\mathbb{V}(\mathbf{X})}. \quad (2.65)$$

Using (2.63) we can rewrite the variance as

$$\begin{aligned} \mathbb{V}(\mathbf{X}) &= \mathbb{E}(|\mathbf{X} - \mathbb{E}(\mathbf{X})|^2) \\ &= \int_{\mathbb{R}^n} |\mathbf{x} - \mathbb{E}(\mathbf{X})|^2 g(\mathbf{x}) d^n \mathbf{x} \\ &= \int_{\mathbb{R}^n} (|\mathbf{x}|^2 - 2\mathbf{x} \cdot \mathbb{E}(\mathbf{X}) + |\mathbb{E}(\mathbf{X})|^2) g(\mathbf{x}) d^n \mathbf{x} \\ &= \mathbb{E}(|\mathbf{X}|^2) - |\mathbb{E}(\mathbf{X})|^2. \end{aligned} \quad (2.66)$$

From this we deduce that $\mathbb{V}(h(\mathbf{X}))$ is also well-defined.

We shall frequently use the term independent random variables. Roughly speaking, this means that the probability for an event of a random variable \mathbf{X}_1 is unrelated to events of a second random variable \mathbf{X}_2 . More precisely, let $\mathbf{X}_1 = (\mathbb{R}^l, g_1)$ and $\mathbf{X}_2 = (\mathbb{R}^m, g_2)$, then we denote by $\mathbf{X} = (\mathbb{R}^{l+m}, g)$ a new random variable with probability

$$P_{\mathbf{X}}(A) = P(\mathbf{X}_1 \in A_1, \mathbf{X}_2 \in A_2) = \int_A g(\mathbf{x}_1, \mathbf{x}_2) d^{l+m} \mathbf{x}, \quad (2.67)$$

where $A = A_1 \times A_2$. The random variables \mathbf{X}_1 and \mathbf{X}_2 are said to be *independent* if

$$P(\mathbf{X}_1 \in A_1, \mathbf{X}_2 \in A_2) = P(\mathbf{X}_1 \in A_1) P(\mathbf{X}_2 \in A_2), \quad (2.68)$$

or, in terms of PDFs, $g(\mathbf{x}_1, \mathbf{x}_2) = g_1(\mathbf{x}_1)g_2(\mathbf{x}_2)$. For independent real-valued random variables X_1, \dots, X_n one has

$$\mathbb{E}(X_1 \dots X_n) = \mathbb{E}(X_1) \dots \mathbb{E}(X_n), \quad (2.69)$$

$$\mathbb{V}(X_1 + \dots + X_n) = \mathbb{V}(X_1) + \dots + \mathbb{V}(X_n) \quad (\text{Bienaym\'e's theorem}). \quad (2.70)$$

2.3.2. Estimators

In practice sometimes the PDF of a random variable of interest is not known exactly; observables which are functions of this random variable must then be estimated from sample data. The correct way to do this in statistics is via *estimators*, which are themselves functions of random variables.

Suppose that $\mathbf{X} = (\mathbb{R}^n, g)$ is a random variable of which g is not known. Further, let $h : \mathbb{R}^n \rightarrow \mathbb{R}^d$, $d \geq 1$ stand for a (possibly vector-valued) function and suppose an observable of interest θ is given by

$$\theta_M = \mathbb{E}(h(\mathbf{X})). \quad (2.71)$$

In order to approximate θ_M , let $(\mathbf{X}_i)_{i=1\dots N}$ stand for a vector of N independent random variables $\mathbf{X}_i = (\mathbb{R}^n, g)$, thus distributed according to g , and define the *sample mean*

$$\bar{\theta}_M := \frac{1}{N} \sum_{i=1}^N h(\mathbf{X}_i). \quad (2.72)$$

2. Theoretical aspects

This is a function of the random variables $(\mathbf{X}_i)_i$ and an estimator for the expected value (2.71). The *bias* of an estimator $\bar{\theta}$ is defined as $bias(\bar{\theta}) := \theta - \mathbb{E}(\bar{\theta})$. An estimator is called unbiased if its bias is zero, which is clearly the case for the sample mean,

$$\mathbb{E}(\bar{\theta}_M) = \frac{1}{N} \sum_{i=1}^N \mathbb{E}(h(\mathbf{X}_i)) = \frac{1}{N} \sum_{i=1}^N \mathbb{E}(h(\mathbf{X})) = \mathbb{E}(h(\mathbf{X})) = \theta_M , \quad (2.73)$$

since the \mathbf{X}_i are distributed like \mathbf{X} . Using Bienaymé's theorem (2.70) one can show that an unbiased estimator for the observable

$$\theta_V = \mathbb{V}(h(\mathbf{X})) \quad (2.74)$$

is given by

$$\bar{\theta}_V := \frac{1}{N-1} \sum_{i=1}^N |h(\mathbf{X}) - \bar{\theta}_M|^2 = \frac{1}{N-1} \sum_{i=1}^N \left| h(\mathbf{X}) - \frac{1}{N} \sum_{i=1}^N h(\mathbf{X}_i) \right|^2 . \quad (2.75)$$

Remark that using $1/N$ in front of the sum would also yield an estimator for the variance, but this estimator would be biased.

The *mean square error* (MSE) of an estimator $\bar{\theta}$ approximating an observable θ reads

$$MSE(\bar{\theta}) := \mathbb{E}(|\bar{\theta} - \theta|^2) . \quad (2.76)$$

A straightforward computation yields

$$\begin{aligned} MSE(\bar{\theta}) &= \mathbb{E}(|\bar{\theta} - \theta|^2) = \mathbb{E}(|\bar{\theta}|^2) - 2\mathbb{E}(\bar{\theta}) \cdot \theta + |\theta|^2 \\ &= \mathbb{E}(|\bar{\theta}|^2) - |\mathbb{E}(\bar{\theta})|^2 + |\mathbb{E}(\bar{\theta})|^2 - 2\mathbb{E}(\bar{\theta}) \cdot \theta + |\theta|^2 \\ &= \mathbb{V}(\bar{\theta}) + |\theta - \mathbb{E}(\bar{\theta})|^2 \\ &= \mathbb{V}(\bar{\theta}) + |bias(\bar{\theta})|^2 . \end{aligned} \quad (2.77)$$

The *root mean square error* (RMS) of an estimator is the square root of the MSE. For an unbiased estimator, it follows that the RMS is the standard deviation $RMS(\bar{\theta}) = \sigma(\bar{\theta})$. For the sample mean (2.72) we can use Bienaymé's theorem (2.70) to compute

$$\mathbb{V}(\bar{\theta}_M) = \mathbb{V}\left(\frac{1}{N} \sum_{i=1}^N h(\mathbf{X}_i)\right) = \frac{1}{N^2} \mathbb{V}\left(\sum_{i=1}^N h(\mathbf{X}_i)\right) = \frac{1}{N} \mathbb{V}(h(\mathbf{X})) , \quad (2.78)$$

since the $(\mathbf{X}_i)_i$ are distributed like \mathbf{X} . We conclude that

$$RMS(\bar{\theta}_M) = \frac{\sigma(\theta)}{\sqrt{N}} . \quad (2.79)$$

This is the statistical error found in MC simulations when working with the sample mean as an estimator for observables. Two things are noteworthy: the convergence rate with $1/\sqrt{N}$ and the fact that the error is proportional to the standard deviation of the observable θ . Choosing thus in a clever way the observable so to minimize σ can lead to a reduced error in the simulations - this is the purpose of the control variates introduced in the Numerical Methods section.

Part II.

Body: what was done for the thesis

3. Numerical Methods

In this chapter we present the numerical methodology. At first, we introduce a particle-in-cell (PIC) solver for the Vlasov-Poisson system, based on a regular, uniform grid. The Monte-Carlo interpretation of the density computation and the notion of a control variate will be discussed in detail. In the second part we present an essentially-non-oscillatory (ENO) finite volume scheme for the fluid moment equations. The coupling of PIC-ENO is discussed in the last chapter.

3.1. The kinetic solver

3.1.1. Principle of a PIC solver

The VP system (2.1) is solved using a grid based particle-in-cell method, which uses a grid, shown in fig. 3.1, for the electric field computation:

$$x_{j-\frac{1}{2}} = j\Delta x, \quad j = 0, \dots, N_x - 1, \quad \Delta x = \frac{L}{N_x}. \quad (3.1)$$

Here, L is the length of the domain, N_x is the number of discretization points and $C_j = [x_{j-\frac{1}{2}}, x_{j+\frac{1}{2}}]$ is the j -th cell with left boundary (or left interface) at $x_{j-\frac{1}{2}}$ and right boundary at $x_{j+\frac{1}{2}}$. We will apply the Fourier spectral method to compute the electric field at the interface points, i.e. the vector $(E_{j-\frac{1}{2}})_j$, from the equations in Fourier space,

$$ik\hat{E}_k = 1 - \hat{n}_k \quad k = -\frac{N_x}{2}, \dots, \frac{N_x}{2} - 1, \quad (3.2)$$

where

$$\hat{E}_k = \frac{1}{L} \int_0^L E(x) e^{-ikx} dx, \quad \hat{n}_k = \frac{1}{L} \int_0^L n(x) e^{-ikx} dx, \quad (3.3)$$

stand for the k -th Fourier coefficient of E and n , which are approximated by the discrete Fourier transform (DFT) as

$$\hat{E}_k = \sum_{j=-N_x/2}^{N_x/2-1} E_{j-\frac{1}{2}} e^{-\frac{2\pi i(jk)}{N_x}}, \quad \hat{n}_k = \sum_{j=-N_x/2}^{N_x/2-1} n_{j-\frac{1}{2}} e^{-\frac{2\pi i(jk)}{N_x}}. \quad (3.4)$$

The solution of $(E_{j-\frac{1}{2}})_j$ at the interfaces is given by

$$E_{j-\frac{1}{2}} = \sum_{j=-N_x/2}^{N_x/2-1} \hat{E}_k e^{-\frac{2\pi i(jk)}{N_x}}. \quad (3.5)$$

We set $\hat{E}_0 = 0$ (zero mean condition) to get a unique solution.

3. Numerical Methods

To solve the Vlasov equation, we shall use the fact that f is constant along the characteristics, i.e. $f(t, \mathcal{X}(t), \mathcal{V}(t)) = f(0, \mathcal{X}(0), \mathcal{V}(0))$. This allows us to integrate the partial differential equation that is Vlasov by solving a large number of ordinary differential equations for the so called *markers* (x_k, v_k) , $k = 0, \dots, N_k$:

$$\frac{dx_k}{dt} = v_k, \quad x_k(0) = x_k^0, \quad (3.6a)$$

$$\frac{dv_k}{dt} = -E(t, x_k(t)), \quad v_k(0) = v_k^0. \quad (3.6b)$$

The *marker distribution* $g : [0, T] \times \Omega \rightarrow \mathbb{R}$ is assumed to satisfy the same Vlasov equation as the plasma distribution function f , hence

$$\begin{cases} \partial_t g + v \partial_x g - E \partial_v g = 0, \\ g(t = 0, x, v) = g_0(x, v), \end{cases} \quad (3.7)$$

with two differences:

1. The marker distribution is normalized to one: $\int g \, dx \, dv = 1$.
2. The initial condition can be different: $g_0 \neq f_0$.

The initial states (x_k^0, v_k^0) in (3.6) are drawn according to g_0 . In order to "push" the *markers* in time, let us introduce the following time grid:

$$t^n = n\Delta t, \quad n = 0, \dots, N_t, \quad \Delta t = \frac{T}{N_t - 1}. \quad (3.8)$$

The *markers* are then pushed from time t^n to time t^{n+1} with the Verlet scheme, which is a three-step process:

$$\begin{aligned} 1) \quad & v_k^{n+\frac{1}{2}} = v_k^n - \frac{\Delta t}{2} E(t^n, x_k^n), \\ 2) \quad & x_k^{n+1} = x_k^n + \Delta t v_k^{n+\frac{1}{2}}, \\ 3) \quad & v_k^{n+1} = v_k^{n+\frac{1}{2}} - \frac{\Delta t}{2} E(t^{n+1}, x_k^{n+1}). \end{aligned}$$

Remark that between the steps 2) and 3) the electric field is to be updated.

3.1.2. Monte Carlo integration

The critical point of every PIC solver is the *particle-mesh coupling*. The problem is two fold:

- (A) Given the *markers* $(x_k(t^n), v_k(t^n), k = 1, \dots, N_k)$, at time t^n , compute the density $n(t^n, x_{j-\frac{1}{2}})$ at the interface points $(x_{j-\frac{1}{2}})_j$.
- (B) Given the electric field at the interface points, $(E_{j-\frac{1}{2}})_j$, compute the electric field at the particle positions.

3. Numerical Methods

The Monte Carlo method is used to calculate the density in problem (A). The exact expression for the density at point $x_{j-\frac{1}{2}}$ reads

$$n(t, x_{j-\frac{1}{2}}) = \int f(t, x_{j-\frac{1}{2}}, v) dv. \quad (3.10)$$

We can add and subtract any term, so we add and subtract a function $\mathcal{M} = \mathcal{M}(t, x, v)$. It is a function on the phase space and will act as a control variate in Monte-Carlo integration. Then (3.10) becomes:

$$n(t, x_{j-\frac{1}{2}}) = \int [f(t, x_{j-\frac{1}{2}}) - \mathcal{M}(t, x_{j-\frac{1}{2}}, v)] dv + \int \mathcal{M}(t, x_{j-\frac{1}{2}}, v) dv. \quad (3.11)$$

In what follows we denote by

$$n_0(t, x_{j-\frac{1}{2}}) := \int \mathcal{M}(t, x_{j-\frac{1}{2}}, v) dv$$

the density related to \mathcal{M} and assume it to be known. In order to compute the density from the cloud of markers, f must be smoothed with a shape function $S : [0, L] \rightarrow \mathbb{R}$, which is normalized, $\int_0^L S dx = 1$. Then we define the smoothed density as

$$n_s(t, x_{j-\frac{1}{2}}) := \int [S(x - x') f(t, x', v') - \mathcal{M}(t, x_{j-\frac{1}{2}}, v')] dx' dv' + n_0(t, x_{j-\frac{1}{2}}). \quad (3.12)$$

Remark that $\mathcal{M}(x_{j-\frac{1}{2}}, v')$ is evaluated at x instead of x' , and thus not convoluted with S . For $S(x) \rightarrow \delta(x)$, the Dirac distribution, the exact density is recovered. Using the marker distribution function g , (3.12) can be written as

$$n_s(t, x_{j-\frac{1}{2}}) = \int S(x - x') \frac{f(t, x', v') - \mathcal{M}(t, x_{j-\frac{1}{2}}, v')}{g(t, x', v')} g(t, x', v') dx' dv' + n_0(t, x_{j-\frac{1}{2}}). \quad (3.13)$$

In that sense $n_{j-\frac{1}{2}}^n := n_s(t^n, x_{j-\frac{1}{2}})$ is an expectation value,

$$n_{j-\frac{1}{2}}^n = \mathbb{E} \left[S(x_{j-\frac{1}{2}} - X) \frac{f(t, X, V) - \mathcal{M}(t, x_{j-\frac{1}{2}}, V)}{g(t, X, V)} \right] + n_0(t, x_{j-\frac{1}{2}}), \quad (3.14)$$

where (X, V) is a time-dependent random variable with PDF $g(t, x, v)$. Using the sample mean from section 2.3.2, an estimate for $n_{j-\frac{1}{2}}^n$ is given by

$$n_{j-\frac{1}{2}}^n \approx n_{j-\frac{1}{2}}^{\text{PIC}, n} := \frac{1}{N_k} \sum_{k=1}^{N_k} S(x_{j-\frac{1}{2}} - x_k(t)) \left[w_k - \frac{\mathcal{M}(t^n, x_{j-\frac{1}{2}}, v_k)}{g_0(x_k^0, v_k^0)} \right] + n_0(t, x_{j-\frac{1}{2}}), \quad (3.15)$$

where we introduce the weights w_k as

$$w_k := \frac{f(t, x_k(t), v_k(t))}{g(t, x_k(t), v_k(t))} = \frac{f_0(x_k^0, v_k^0)}{g_0(x_k^0, v_k^0)}. \quad (3.16)$$

Due to the last equality the weights are constant in time. Recall that the initial x_k^0 and v_k^0 are drawn from $g_0(x, v)$. Here both f and g satisfy the Vlasov equation, and are thus conserved along the characteristics. The whole process of computing the density on the grid is called charge deposition.

3.1.3. Electric field at marker positions

Let us now turn our attention to the problem (B), given the electric field at the interface points, $(E_{j-\frac{1}{2}})_j$, computing the electric field at the particle positions. First we define a smoothed electric field E_s by convolution of the electric field E with a shape function S . We then approximate E_s via the trapezoidal quadrature rule,

$$E_s(t, x_{j-\frac{1}{2}}) := \int E(t, x') S(x_{j-\frac{1}{2}} - x') dx' \approx \Delta x \sum_i E(t, x_{i-\frac{1}{2}}) S(x_{j-\frac{1}{2}} - x_{i-\frac{1}{2}}). \quad (3.17)$$

It is important to use the same shape function S as in the definition of n_s to have a good stability of the scheme. In our scheme S will be a spline of degree three with $\text{supp } S(x) = [-2\Delta x, 2\Delta x]$.

3.1.4. PIC method cycle

Let us state here in brief one cycle of our PIC algorithm:

1. Assume x_k^n, v_k^n, E^n are known at time t^n .
2. Push markers, part 1:

Advance the velocities using Verlet scheme: first advance the velocities by half time step, and then advance the particle positions by one time step:

$$\begin{aligned} v_k^{n+\frac{1}{2}} &= v_k^n - \frac{\Delta t}{2} E(t^n, x_k^n), \\ x_k^{n+1} &= x_k^n + \Delta t v_k^{n+\frac{1}{2}}, \quad k = 1, \dots, N_k. \end{aligned}$$

3. Charge deposition: find the particle density using (3.15).
4. Electric field solve via the formulas (3.2)-(3.5).
5. Electric field at particle positions from (3.17).
6. Push markers, part 2:

After the electric field $E(t^{n+1}, x_k^{n+1})$ has been computed for all $k = 1, \dots, N_k$, advance the velocities a half time step:

$$v_k^{n+1} = v_k^{n+\frac{1}{2}} - \frac{\Delta t}{2} E(t^{n+1}, x_k^{n+1}).$$

3.2. The fluid solver

Plasmas can be thought of as electrically conducting fluids, capable of carrying current and exhibiting collective behavior. Therefore, plasmas can also be modeled as fluids, characterized by their macroscopic quantities such as density, velocity and temperature. The fluid description is based on the assumption that due to collisions, the plasma returns quickly to the thermodynamic equilibrium and hence can be modeled as a fluid. The fluid description of the plasma takes the conservative form of hyperbolic differential equations and the finite volume method [8] is the most widely used scheme to solve such equations.

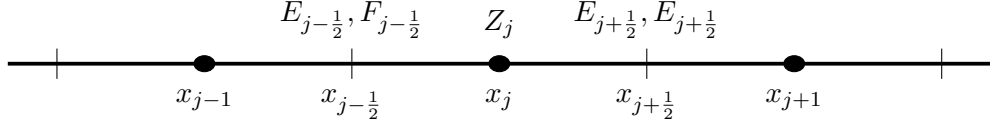


Figure 3.1.: The grid with the cell centers at x_j and cell interfaces at $x_{j\pm\frac{1}{2}}$.

3.2.1. Finite volume method

Let us recall that the Euler equations can be written in the conservative form

$$\partial_t Z + \partial_x F = 0, \quad (3.19)$$

with

$$Z = \begin{pmatrix} n \\ nu \\ w \end{pmatrix}, \quad F = \begin{pmatrix} nu \\ nu^2 + p \\ wu + pu \end{pmatrix}, \quad (3.20)$$

where F is the flux function. Our aim is to apply a finite volume method to (3.19). For this, the domain is discretized into cells according to the grid depicted in Fig. 3.1. Each cell $C_j = [x_{j-\frac{1}{2}}, x_{j+\frac{1}{2}}]$ has left and right boundaries through which the flux can enter the cell. Integrating (3.19) with respect to x over the j -th cell gives:

$$\partial_t \int_{x_{j-\frac{1}{2}}}^{x_{j+\frac{1}{2}}} Z(t, x) dx + \left[F\left(Z(t, x_{j+\frac{1}{2}})\right) - F\left(Z(t, x_{j-\frac{1}{2}})\right) \right] = 0. \quad (3.21)$$

If we define cell averages and as

$$Z_j(t) := \frac{1}{\Delta x} \int_{x_{j-\frac{1}{2}}}^{x_{j+\frac{1}{2}}} Z(t, x) dx,$$

eq (3.21) becomes

$$\partial_t Z_j(t) + \frac{1}{\Delta x} \left[F\left(Z(t, x_{j+\frac{1}{2}})\right) - F\left(Z(t, x_{j-\frac{1}{2}})\right) \right] = 0. \quad (3.22)$$

This is still an exact evolution equation for the cell averages. To obtain the numerical solution of (3.22), the flux terms are to be approximated, since $Z(t, x_{j\pm\frac{1}{2}})$ are not known, only the cell averages $Z_j(t)$ are known. The fluxes at the interfaces can be approximated by different methods. One such method is the Lax-Friedrichs method which approximates fluxes as

$$F(Z(t, x_{j-\frac{1}{2}})) \approx F_{j-\frac{1}{2}}(t) := \frac{1}{2} \left[F(t, Z_{j-\frac{1}{2}}^-) + F(t, Z_{j-\frac{1}{2}}^+) \right] - \frac{|\lambda_{j-\frac{1}{2}}|}{2} (Z_{j-\frac{1}{2}}^+ - Z_{j-\frac{1}{2}}^-), \quad (3.23)$$

for $j = 0, \dots, N_{x-1}$. Here,

$$Z^-(t, x_{j-\frac{1}{2}}) = \lim_{x \rightarrow x_{j-\frac{1}{2}}^-} p_{j-1}(t, x), \quad (3.24)$$

and

$$Z^+(t, x_{j-\frac{1}{2}}) = \lim_{x \rightarrow x_{j-\frac{1}{2}}^+} p_j(t, x), \quad (3.25)$$

where $p_j \in \mathbb{R}[x]_{k-1}$, $k \geq 1$, are polynomials of degree $k-1$, reconstructed from the cell averages $(Z_j)_j$. Also, $\lambda_{j-\frac{1}{2}}$ are the maximum eigenvalues of Jacobian matrix $\frac{\partial F}{\partial Z}$ at the interfaces, with

$$\lambda_{j-\frac{1}{2}} = \max(u^\pm, u^\pm + \sqrt{3T^\pm}, u^\pm - \sqrt{3T^\pm})_{j-\frac{1}{2}}. \quad (3.26)$$

Here, \pm refer to left and right limits as in (3.24)-(3.25) and $T = \frac{p}{n}$.

3.2.2. ENO reconstruction scheme

High order reconstruction schemes are available. One such scheme is the essentially non oscillatory (ENO) scheme [9]. The goal is to compute values of $Z(x)$ at the interface points $x_{j \pm \frac{1}{2}}$, where only the cell averages $(Z_j)_j$ are known. The function $Z(x)$ can be approximated, in each cell C_j , by a polynomial $p_j(x)$ of degree $k-1$, where $p_j(x)$ is k -th order accurate approximation to the function $Z(x)$ in the cell C_j , thus

$$p_j(x) = Z(x) + O(\Delta x^k), \quad x \in C_j. \quad (3.27)$$

This way the function $Z(x)$ can be approximated at cell interfaces as:

$$Z_{j+\frac{1}{2}}^- = p_j(x_{j+\frac{1}{2}}), \quad Z_{j-\frac{1}{2}}^+ = p_j(x_{j-\frac{1}{2}}), \quad j = 0, \dots, N_x - 1. \quad (3.28)$$

In this way two values are calculated at each interface:

$$Z_{j-\frac{1}{2}}^- = p_{j-1}(x_{j-\frac{1}{2}}), \quad Z_{j-\frac{1}{2}}^+ = p_j(x_{j-\frac{1}{2}}).$$

For a k -th order accurate reconstruction, the cell averages of p_j and Z have to be equal on k neighboring cells, including C_j . This yields enough equations to uniquely define $p_j \in \mathbb{R}[x]_{k-1}$. The simplest case $k=1$ (Rusanov scheme) is trivial, $p_j(x) = Z_j = \text{const}$. The first non trivial case $k=2$ (MUSCL scheme) is discussed next. Our hybrid algorithm runs with $k=4$.

3.2.3. MUSCL scheme

In the ENO scheme for $k=2$, the reconstruction of $Z(t, x)|_j$ from the cell averages $(Z_j)_j$ can be computed by polynomial expression of first order,

$$p_j(t, x)|_j = a_{j,0} + a_{j,1}(x - x_j). \quad (3.29)$$

The cell average becomes

$$\bar{p}_j(t) = \frac{1}{\Delta x} \int_{x_{j-\frac{1}{2}}}^{x_{j+\frac{1}{2}}} p_j(t, x) dx = a_{j,0}.$$

The derivative of (3.29) is given by

$$\frac{\partial p_j}{\partial x} = a_{j,1}.$$

Then the equation (3.29) becomes

$$p_j(t, x)|_j = \bar{p}_j(t) + \frac{\partial p_j}{\partial x} \Big|_j (x - x_j). \quad (3.30)$$

Now, the slope $\frac{\partial p_j}{\partial x} \Big|_j$ is approximated by

$$\frac{\partial p_j}{\partial x} \Big|_j \approx \text{minmod} \left(\frac{\partial Z^+}{\partial x}, \frac{\partial Z^-}{\partial x} \right), \quad (3.31)$$

where,

$$\frac{\partial Z^+}{\partial x} := \frac{Z_{j+1} - Z_j}{\Delta x}, \quad \frac{\partial Z^-}{\partial x} := \frac{Z_j - Z_{j-1}}{\Delta x}. \quad (3.32)$$

The minmod-function is defined as:

$$\text{minmod}(a, b) = \begin{cases} a & \text{if } |a| \leq |b|, ab \geq 0 \\ b & \text{if } |a| > |b|, ab \geq 0 \\ 0 & \text{if } ab < 0. \end{cases} \quad (3.33)$$

3.2.4. Discretization in time

Once the ENO-finite volume scheme is in place, equation (3.22) can be discretized in time using a similarly accurate time discretization. Runge-Kutta (RK) methods are our methods of choice. For a k-th order ENO reconstruction, we shall use a standard k-th order RK scheme. In order to have a stable scheme, we choose the time step Δt according to the CFL condition

$$\Delta t = \frac{0.5 \Delta x}{\max_j |\lambda_{j-\frac{1}{2}}|}, \quad (3.34)$$

where $\lambda_{j-\frac{1}{2}}$ are eigenvalue given by (3.26).

3.3. Hybrid scheme

For the hybrid scheme we consider the fluid system with additional terms composed of heat flux and electric field source terms. The full system is given by

$$\begin{cases} \frac{\partial f}{\partial t} + v \frac{\partial f}{\partial x} - E \frac{\partial f}{\partial v} = 0, \\ -\frac{\partial^2 \phi}{\partial x^2} = 1 - n^*, \quad E = -\frac{\partial \phi}{\partial x}, \\ \frac{\partial n}{\partial t} + \frac{\partial(n u)}{\partial x} = 0, \\ \frac{\partial(n u)}{\partial t} + \frac{\partial(n u^2 + p)}{\partial x} = -nE, \\ \frac{\partial w}{\partial t} + \frac{\partial(w u + p u)}{\partial x} = -nuE - \frac{\partial q}{\partial x}. \end{cases} \quad (3.35)$$

3. Numerical Methods

Here, n^* is the electron density, computed either from the *markers* as in (3.15) or taken as the solution of the fluid equations, leading to different hybrid schemes. Moreover, q is the *heat flux* given by

$$q(t, x) = \frac{1}{2} \int (v - u(t, x))^3 f(t, x, v) dv.$$

In conservative form the fluid system becomes

$$\partial_t Z + \partial_x F = S, \quad (3.36)$$

where

$$Z = \begin{pmatrix} n \\ nu \\ w \end{pmatrix}, \quad F = \begin{pmatrix} nu \\ nu^2 + p \\ wu + pu \end{pmatrix}, \quad S = \begin{pmatrix} 0 \\ -nE \\ -nuE - \partial_x q \end{pmatrix}. \quad (3.37)$$

We shall use the Monte-Carlo technique from section 3.1.2 to compute the heat flux, similar to the computation of the density (3.15). Again, adding and subtracting a function $\mathcal{M} = \mathcal{M}(t, x, v)$ for the purpose of variance reduction leads to

$$q(t, x_{j-\frac{1}{2}}) = \frac{1}{2} \int (v - u(t, x_{j-\frac{1}{2}}))^3 (f(t, x_{j-\frac{1}{2}}, v) - \mathcal{M}(t, x_{j-\frac{1}{2}}, v)) dv + q_0(t, x_{j-\frac{1}{2}}), \quad (3.38)$$

where

$$q_0(t, x_{j-\frac{1}{2}}) := \frac{1}{2} \int (v_k - u(t, x_{j-\frac{1}{2}}))^3 \mathcal{M}(t, x_{j-\frac{1}{2}}, v) dv \quad (3.39)$$

denotes the heat flux related to \mathcal{M} . We define the smoothed heat flux q_s to be

$$\begin{aligned} q_s(t, x_{j-\frac{1}{2}}) &:= \frac{1}{2} \int [S(x - x')(v' - u(t, x_{j-\frac{1}{2}}))^3 f(t, x', v') - \mathcal{M}(t, x_{j-\frac{1}{2}}, v')] dx' dv' \\ &\quad + q_0(t, x_{j-\frac{1}{2}}). \end{aligned} \quad (3.40)$$

Remark that u and \mathcal{M} are not convoluted with S . Introducing the PDF g , (3.40) can be written as

$$\begin{aligned} q_s(t, x_{j-\frac{1}{2}}) &= \frac{1}{2} \int S(x_{j-\frac{1}{2}} - x') (v' - u(t, x_{j-\frac{1}{2}}))^3 \frac{f(t, x', v') - \mathcal{M}(t, x_{j-\frac{1}{2}}, v')}{g(t, x', v')} g(t, x', v') dx' dv' \\ &\quad + q_0(t, x_{j-\frac{1}{2}}). \end{aligned} \quad (3.41)$$

By introducing the quantity $q_{j-\frac{1}{2}}^n := q_s(t^n, x_{j-\frac{1}{2}})$, (3.41) can be written as an expectation value,

$$q_{j-\frac{1}{2}}^n = \frac{1}{2} \mathbb{E} \left[S(x_{j-\frac{1}{2}} - X) (V - u(t^n, x_{j-\frac{1}{2}}))^3 \frac{f(t^n, X, V) - \mathcal{M}(t^n, x_{j-\frac{1}{2}}, V)}{g(t^n, X, V)} \right] + q_0(t^n, x_{j-\frac{1}{2}}). \quad (3.42)$$

Using the sample mean we approximate heat flux by $q_{j-\frac{1}{2}}^n \approx q_{j-\frac{1}{2}}^{\text{PIC}}$, with

$$q_{j-\frac{1}{2}}^{\text{PIC}} := \frac{1}{2N_k} \sum_{k=1}^{N_k} S(x_{j-\frac{1}{2}} - x_k(t^n)) (v_k - u(t^n, x_{j-\frac{1}{2}}))^3 \left[w_k - \frac{\mathcal{M}(t^n, x_k, v_k)}{g_0(x_k^0, v_k^0)} \right] + q_0(t^n, x_{j-\frac{1}{2}}), \quad (3.43)$$

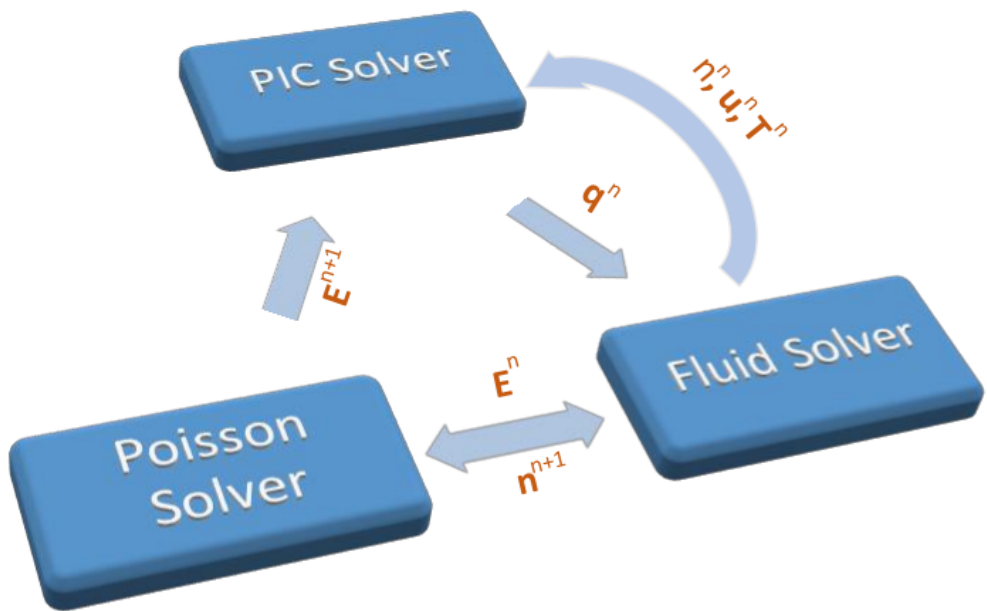


Figure 3.2.: Computing strategy for the hybrid scheme: the updated fluid density n^{n+1} is used to compute the new electric field E^{n+1} , which is then input to the PIC solver.

where the weights w_k are given by (3.16).

An illustration of the proposed hybrid scheme can be seen in the Fig. 3.2. The variables n , u and T go from fluid solver to PIC solver to calculate the local Maxwellian \mathcal{M} . The q is computed with the PIC solver using (3.43). Fluid solver uses the q and electric field E to solve the closed system (3.36)-(3.37). Once the fluid system is solved, the updated density from the fluid solver is used by the Poisson solver to compute the electric field. Finally the PIC solver uses the updated electric field to advance the markers.

The cycle for the hybrid method becomes:

1. Assume $x_k^n, v_k^n, E^n, n^n, (nu)^n, w^n$ are known at time t^n .
2. Calculate Δt using the CFL condition (3.34).
3. Push markers, part 1:

3. Numerical Methods

Advance the velocities using Verlet scheme: first advance the velocities by half time step, and then advance the particle positions by one time step:

$$v_k^{n+\frac{1}{2}} = v_k^n - \frac{\Delta t}{2} E(t^n, x_k^n),$$

$$x_k^{n+1} = x_k^n + \Delta t v_k^{n+\frac{1}{2}}, \quad k = 1, \dots, N_k.$$

4. *Compute q :* estimate the heat flux q using (3.43).
5. *Fluid solve:* use the ENO scheme to compute n^{n+1} , $(nu)^{n+1}$ and w^{n+1} .
6. *Electric field solve* via equations (3.2)-(3.5), with $n^* = n^{n+1}$ from the fluid solver.
7. *Electric field at particle positions* via equation (3.17).
8. *Push markers, part 2:*

After the electric field $E(t^{n+1}, x_k)$ has been computed for all $k = 1, \dots, N_k$, advance the velocities a half time step:

$$v_k^{n+1} = v_k^{n+\frac{1}{2}} - \frac{\Delta t}{2} E(t^{n+1}, x_k^{n+1}).$$

Part III.

Results and Conclusion

4. Simulation Results

4.1. PIC verification tests

Here we present the verification tests for our PIC solver described in the section 3.1, in order to show the correctness the PIC modeling and implementation. At first we perform a linear Landau damping test case and compare the electric field energy with the exact solution obtained from linear analysis presented in section 2.1.5. Moreover, instability growth is verified with the two-stream and the bump-on-tail test case.

4.1.1. Linear Landau damping

For the linear Landau damping test case, we define the Maxwellian $\mathcal{M}(t, x, v) = \mathcal{M}(v)$ as

$$\mathcal{M}(v) := \frac{1}{\sqrt{2\pi}} e^{-\frac{v^2}{2}}. \quad (4.1)$$

Since $\int \mathcal{M}(v) dv = 1$, the equation (3.15) to calculate the density becomes

$$n_{j-1/2}^{\text{PIC},n} := \frac{1}{N_k} \sum_{k=1}^{N_k} S(x_{j-1/2} - x_k^n(t)) \left[w_k^0 - \frac{\mathcal{M}(v_k^n)}{g_0(x_k^0, v_k^0)} \right] + 1. \quad (4.2)$$

The initial condition for the Landau damping is

$$f_0(x, v) = (1 + \epsilon \cos(kx)) \frac{1}{\sqrt{2\pi}} e^{-\frac{v^2}{2}},$$

where ϵ is the small perturbation of the Maxwellian. We use the normal distribution in v as the sampling density, i.e. the initial marker positions x_k^0 and velocities v_k^0 are drawn from

$$g(t=0, x, v) = g_0(x, v) = \frac{1}{L_x} \mathcal{M}(v) = \frac{1}{L_x} \frac{1}{\sqrt{2\pi}} e^{-\frac{v^2}{2}}, \quad L_x = \frac{2\pi}{k}.$$

For the simulation corresponding to Fig. 4.1, the initial perturbation was $\epsilon = 0.001$, $k = 0.5$, and the number of markers was $N_k = 10^5$. We compare the analytical solution's field energy $\int |E|^2 dx$ with the numerical solution and find satisfactory agreement. Fig. 4.2 shows the phase space evolution of the initial perturbation with time. Here we see the filamentation of the phase space density $\delta f = f - \mathcal{M}$ in velocity, because energy form the electric field is being transferred to the particles. This is a good indication of the correctness of the PIC solver.

4.1.2. Two stream instability

For the two stream instability the initial condition used is

$$f_0(x, v) = (1 + \epsilon \cos(kx)) \frac{1}{2\sqrt{2\pi}} \left(e^{-\frac{(v-v_0)^2}{2}} + e^{-\frac{(v+v_0)^2}{2}} \right). \quad (4.3)$$

The initial marker positions x_k^0 and velocities v_k^0 are drawn from

$$g_0(x, v) = \frac{1}{L_x} \frac{1}{2\sqrt{2\pi}} \left(e^{-\frac{(v-v_0)^2}{2}} + e^{-\frac{(v+v_0)^2}{2}} \right), \quad L_x = \frac{2\pi}{k}.$$

For this test case $k = 0.2$, $v_0 = 3.0$ and the initial perturbation was $\epsilon = 0.001$. Fig. 4.3 shows the plot of the initial condition for this test case and Fig. 4.4 shows the initial marker distribution with the number of markers $N_k = 10^5$. The marker distribution is according to the initial condition. We compare the numerical solution of the field energy $\int |E|^2 dx$ with the analytical growth rate $e^{\omega_i t}$ where $\omega_i = 0.2845$ in this case, see Table 2.2. Fig. 4.5 shows that the numerical solution matches the analytical growth rate until $t = 30$. For the later times the expected saturation of the numerical solution due to non-linear effects is observed. The evolution of the phase space density $\delta f = f - \mathcal{M}$ for two stream instability can be seen in Fig. 4.6.

4.1.3. Bump-on-tail instability

The initial condition for the bump-on-tail instability is as follows:

$$f_0(x, v) = (1 + \epsilon \cos(kx)) \left((1 - n_b) \frac{1}{\sqrt{2\pi}} e^{-\frac{v^2}{2}} + \frac{n_b}{\sqrt{2\pi}} e^{-\frac{(v-v_b)^2}{0.5}} \right). \quad (4.4)$$

The initial marker positions and velocities are drawn from

$$g_0(x, v) = \frac{1}{L_x} \left((1 - n_b) \frac{1}{\sqrt{2\pi}} e^{-\frac{v^2}{2}} + \frac{n_b}{\sqrt{2\pi}} e^{-\frac{(v-v_b)^2}{0.5}} \right), \quad L_x = \frac{2\pi}{k}.$$

For the test case presented here, we used $k = 0.3$, $v_b = 4.5$ and $n_b = 0.1$. Fig. 4.7 shows the initial condition for this test case, and Fig. 4.8 shows the initial marker distribution. In Fig. 4.9 we compare the numerical solution of field energy, $\int |E|^2 dx$, with the analytical growth rate $e^{0.198t}$. Again, a good agreement is observed until the non-linear saturation phase.

4.2. Verification of the fluid solver

The verification of our finite volume ENO scheme for the Euler equations proceeds in two steps: first we verify the convergence of the polynomial ENO reconstruction $Z(x)|_j = p_j(x) + O(\Delta x^k)$ for a given scalar function. In the second step we test the full ENO-Runge-Kutta scheme for two test cases, with pressure perturbations. Comparisons to the exact (linearized) solution of section 2.2.3 are provided.

4.2.1. Convergence of ENO reconstruction

The ENO reconstruction $Z(x) = p_j(x) + O(\Delta x^k)$ of the scalar function $Z(x)|_j = \sin(x)$ is tested here. Different orders $k = 2, 3, 4$ of reconstruction are compared for this convergence test. Fig. 4.10 shows that the ENO reconstruction gives the expected convergence rate for every order tested. Shown is the L^1 -error between the exact values at the interfaces and the reconstructed values,

$$\|\sin(x) - p(x)\| := \Delta x \sum_j |\sin(x_{j-\frac{1}{2}}) - p_j(x_{j-\frac{1}{2}})|. \quad (4.5)$$

4.2.2. Convergence of fluid solver

The initial conditions used for this test are

$$n_0 = 1 + \epsilon \cos(kx), \quad u_0 = 1, \quad p_0 = 1 + \epsilon \cos(kx). \quad (4.6)$$

Fig. 4.11 shows the convergence of the fourth order ENO scheme with fourth order RK time discretization for different ϵ . It can be seen that the convergence stalls after a certain error is reached, ϵ^2 to be precise. This is because in deriving the exact solution of the fluid system, we neglected the ϵ^2 -terms. Therefore, once the error reaches ϵ^2 , it stalls. This is the minimum error we can achieve with the linear formulation of the analytical solution.

In Fig. 4.12 we compare different ENO and RK schemes. It can be seen that the fourth order ENO (ENO4) with fourth order RK (RK4) gives near fourth order convergence.

Another test of interest for the fluid equations is the pressure wave. For this test we use the initial conditions

$$n_0 = 1, \quad u_0 = 1, \quad p_0 = 1 + \epsilon e^{\frac{(x-L_x)^2}{0.5}}. \quad (4.7)$$

Fig. 4.13 and Fig. 4.14 show the evolution of the density and pressure profiles respectively, at different instances of time, and for the two different mesh resolutions $N_x = 64$ and $N_x = 256$. The ENO4-RK4 scheme is used for this test. The difference between the coarse and the fine discretization can be seen.

4.3. Hybrid tests

In this section we test the hybrid scheme from Fig. 3.2 in the setting of linear Landau damping cf. section 4.1.1. For the computation of the heat flux $q_{j-\frac{1}{2}}^{\text{PIC},n}$, given in formula (3.43), we define the local Maxwellian $\mathcal{M}(t, x, v)$ as

$$\mathcal{M}(t, x_{j-\frac{1}{2}}, v) := \frac{n(t, x_{j-\frac{1}{2}})}{\sqrt{2\pi T(t, x_{j-\frac{1}{2}})}} e^{-\frac{(v-u(t, x_{j-\frac{1}{2}}))^2}{2T(t, x_{j-\frac{1}{2}})}}.$$

In this case

$$\int (v - u(t, x_{j-\frac{1}{2}}))^3 \mathcal{M}(t, x_{j-\frac{1}{2}}, v) dv = 0, \quad (4.8)$$

because $(v - u(t, x_{j-\frac{1}{2}}))^3$ is an odd function of v and \mathcal{M} is an even function of v .

4. Simulation Results

Our first test is the following: we solve the Vlasov-Poisson system independently of the fluid solution, computing however $(q_{j-\frac{1}{2}}^{\text{PIC},n})_j$ on the side. This allows us to advance the fluid variables with the ENO-RK scheme and, in particular, to compare the fluid densities $n_{j-\frac{1}{2}}^+$ (or $n_{j-\frac{1}{2}}^-$) to the exact density computed from (2.16). For the PIC density (3.15) we use the global Maxwellian (4.1). To derive the initial conditions for the fluid solver we use the definitions of the fluid variables given by (2.17). The initial condition for the fluid density becomes

$$n_0(x) = \int f_0(x, v) dv = \int (1 + \epsilon \cos(kx)) \frac{1}{\sqrt{2\pi}} e^{-\frac{v^2}{2}} dv = 1 + \epsilon \cos(kx). \quad (4.9)$$

For the fluid velocity we derive the initial condition as

$$n_0(x)u_0(x) = \int v f_0(x, v) dv = \int (1 + \epsilon \cos(kx)) \frac{v}{\sqrt{2\pi}} e^{-\frac{v^2}{2}} dv = 0, \quad (4.10)$$

therefore $u_0 = 0$. Similarly the pressure initial condition becomes

$$\begin{aligned} p(x) &= \int f_0(v - u)^2 dv = \int f_0 v^2 dv - n_0 u_0^2 \\ &= \int (1 + \epsilon \cos(kx)) \frac{v^2}{\sqrt{2\pi}} e^{-\frac{v^2}{2}} dv - n_0 u_0^2, \\ &= 1 + \epsilon \cos(kx). \end{aligned} \quad (4.11)$$

We stress again that for this test case we use the PIC density for the electric field computation, $n_{j-\frac{1}{2}}^* = n_{j-\frac{1}{2}}^{\text{PIC}}$. In Fig. 4.15 we plot the L^1 -error

$$\|n_{\text{exact}} - n^-\| = \Delta x \sum_j |n_{\text{exact}} - n_{j-\frac{1}{2}}^-|. \quad (4.12)$$

at the time $t = 4$ for different number of markers. And we compare it with the Monte-Carlo convergence rate $O(\frac{1}{\sqrt{N_k}})$. Fig. 4.17 shows the evolution of the fluid, PIC and analytical density profiles. Since the PIC solver is independent of the fluid solver, the PIC density follows the exact density. Due to noise in the q computation, the fluid density deviates from the exact density after some time.

For the 2nd test we use the fluid density for the electric field computation and this way we have the PIC-fluid coupling. Fig. (4.16) show the convergence of this hybrid scheme. Fig. (4.18) show the evolution of density profiles. In this case we see that after some time the PIC density also starts to deviate from the exact density. Since the electric field is computed with fluid density, any noise in the q computation will effect the PIC density as well.

4.4. Simulation figures

4. Simulation Results

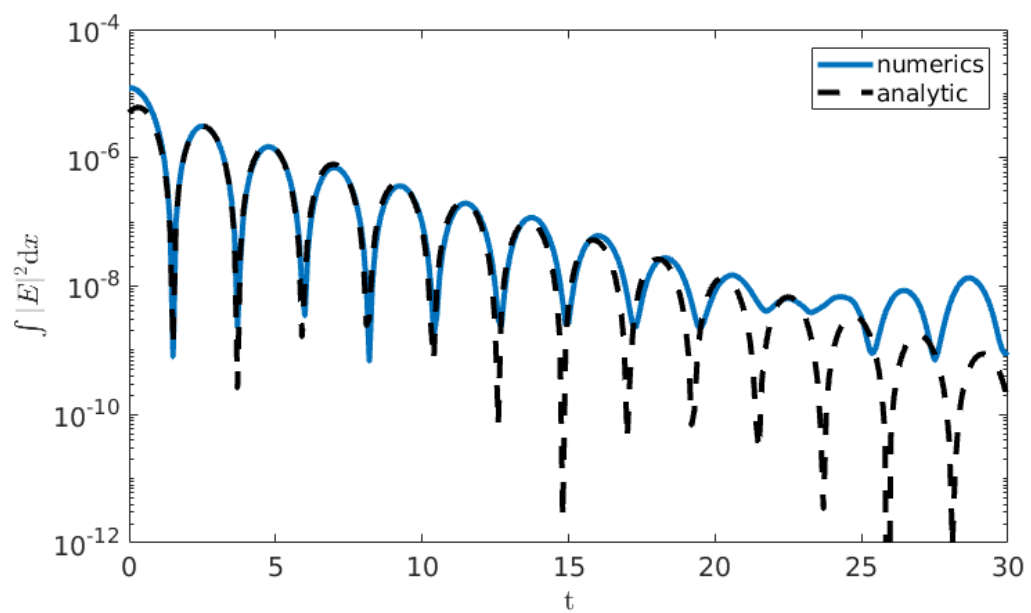


Figure 4.1.: Landau damping test with $k = 0.5$, $\epsilon = 0.001$ and $N_k = 10^5$.

4. Simulation Results

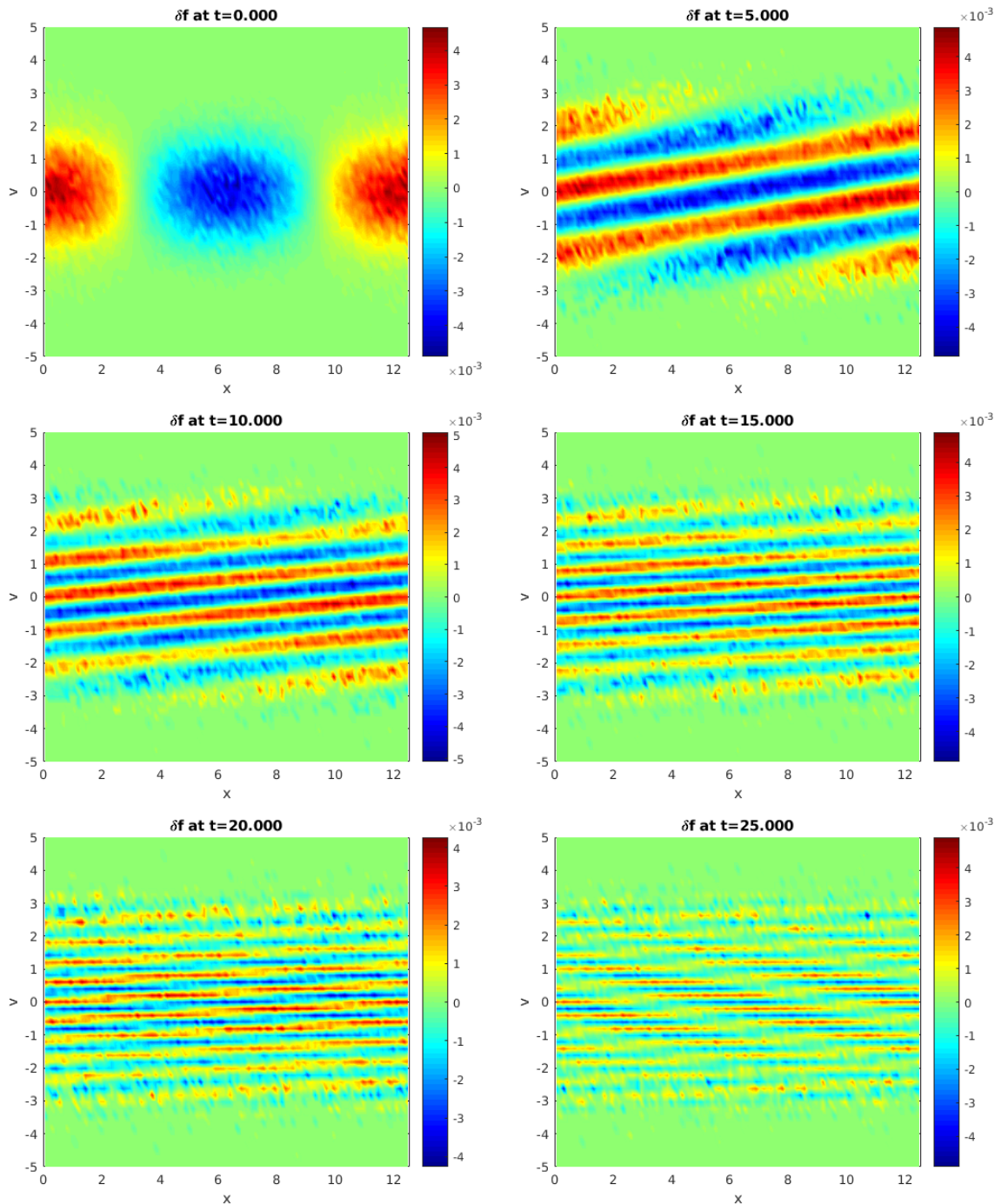


Figure 4.2.: Evolution of the distribution function $\delta f = f - \mathcal{M}$ with respect to time for the linear Landau damping test case with $N_k = 10^5$.

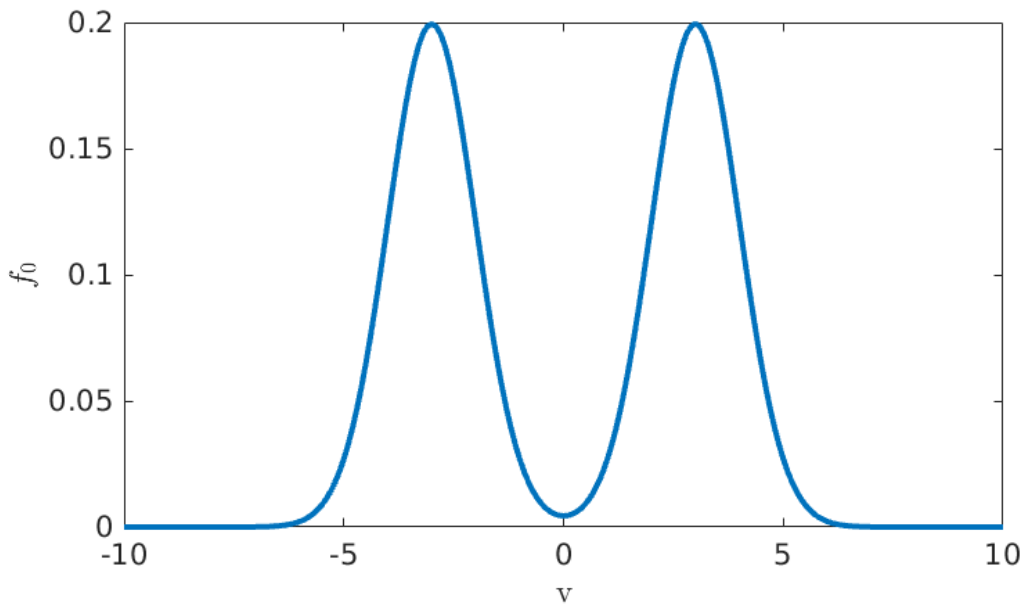


Figure 4.3.: Initial condition for the two-stream instability test cf. (4.3) with $k = 0.2$, $\epsilon = 0.001$, $v_0 = 3.0$.

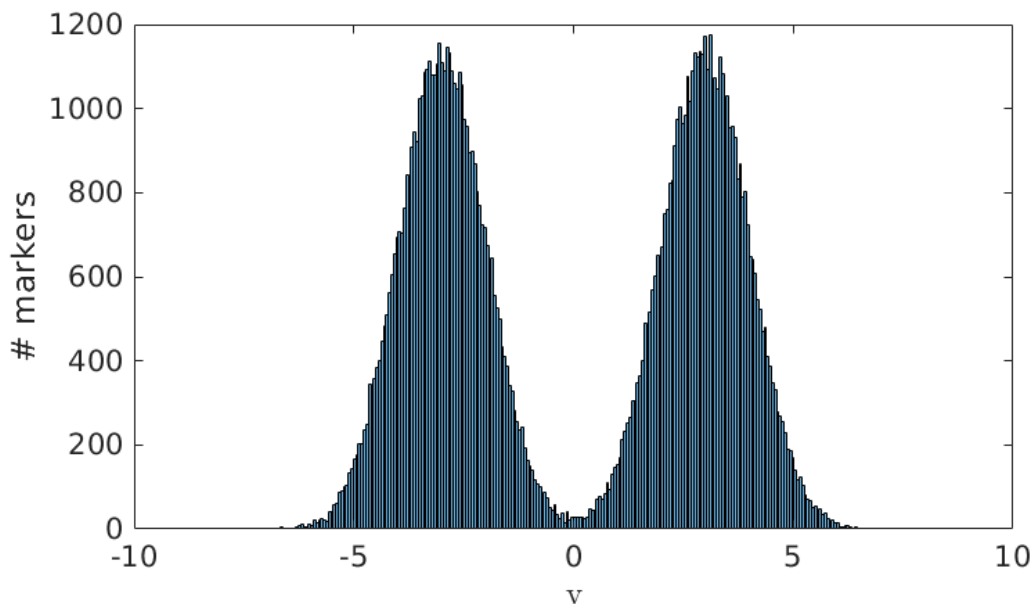


Figure 4.4.: Initial marker distribution for the two-stream instability test with $k = 0.2$, $\epsilon = 0.001$, $v_0 = 3.0$, and $N_k = 10^5$.

4. Simulation Results

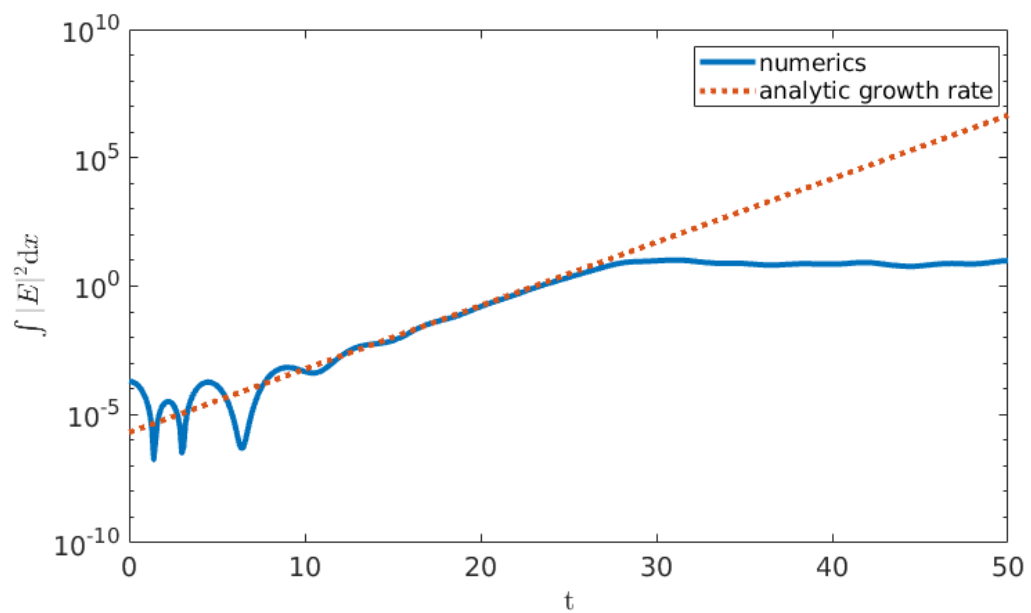


Figure 4.5.: Two-stream instability test with the $k = 0.2$, $\epsilon = 0.001$, $v_0 = 3.0$.

4. Simulation Results

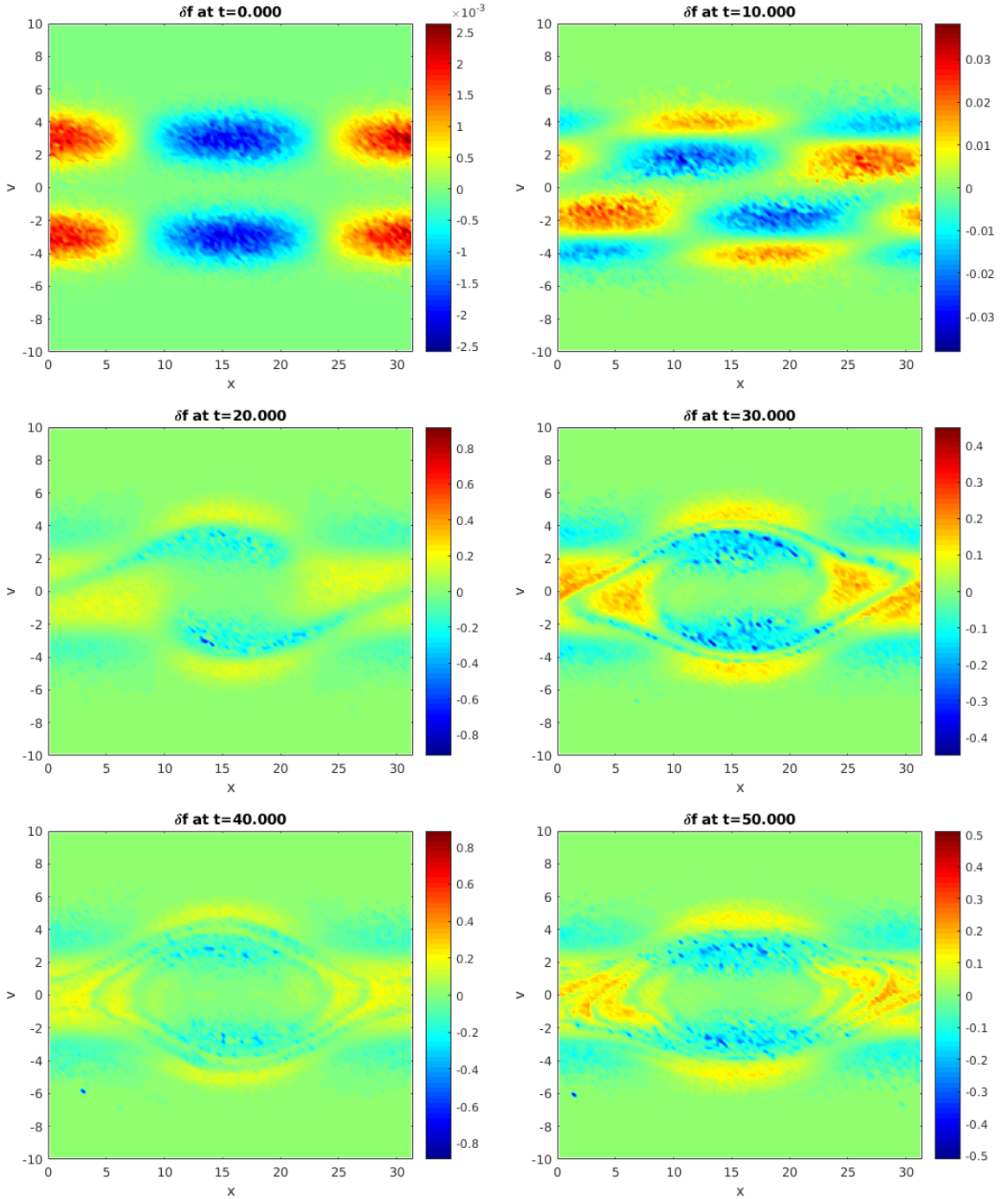


Figure 4.6.: Evolution of the distribution function $\delta f = f - \mathcal{M}$ with respect to time. After 30s, δf is stationary which can be seen in Fig. 4.5 as well.

4. Simulation Results

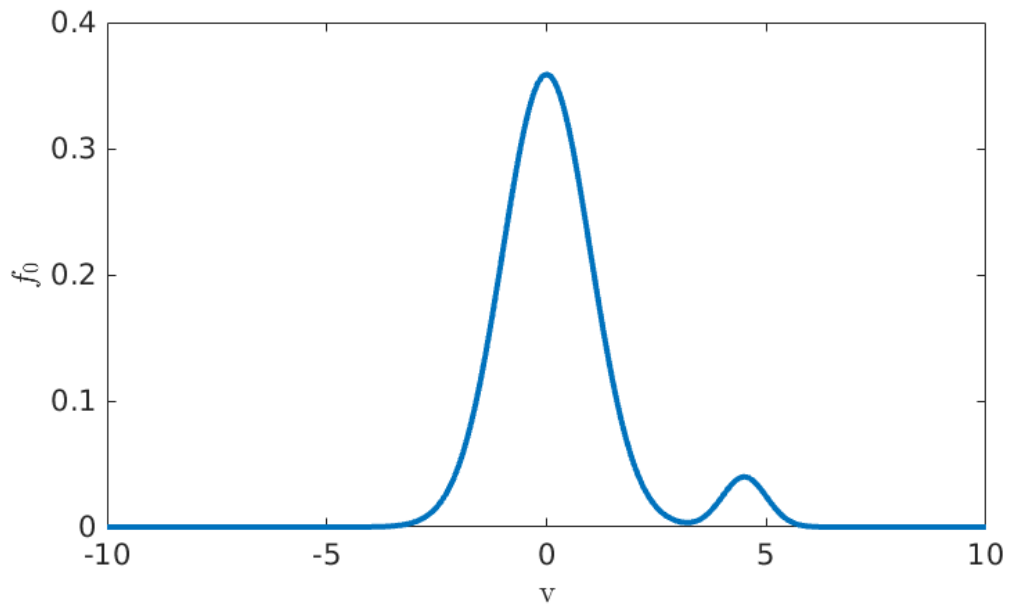


Figure 4.7.: Initial condition for the bump-on-tail instability, cf.(4.4), with $k = 0.3$, $\epsilon = 0.001$, $v_b = 4.5$, $n_b = 0.1$, and $N_k = 10^5$.

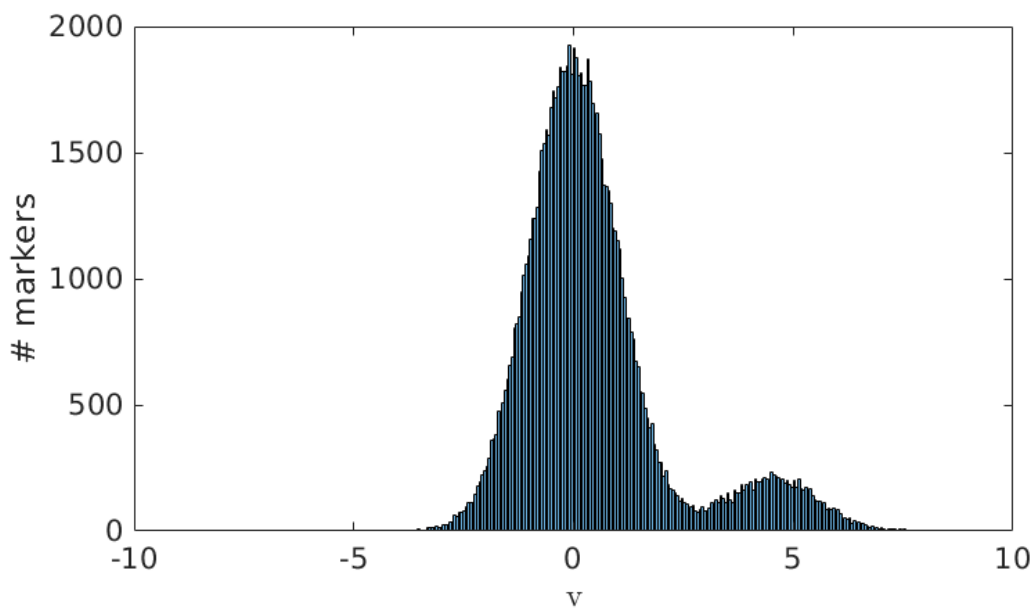


Figure 4.8.: Marker initialization for the bump-on-tail instability, with $k = 0.3$, $\epsilon = 0.001$, $v_b = 4.5$ and $n_b = 0.1$.

4. Simulation Results

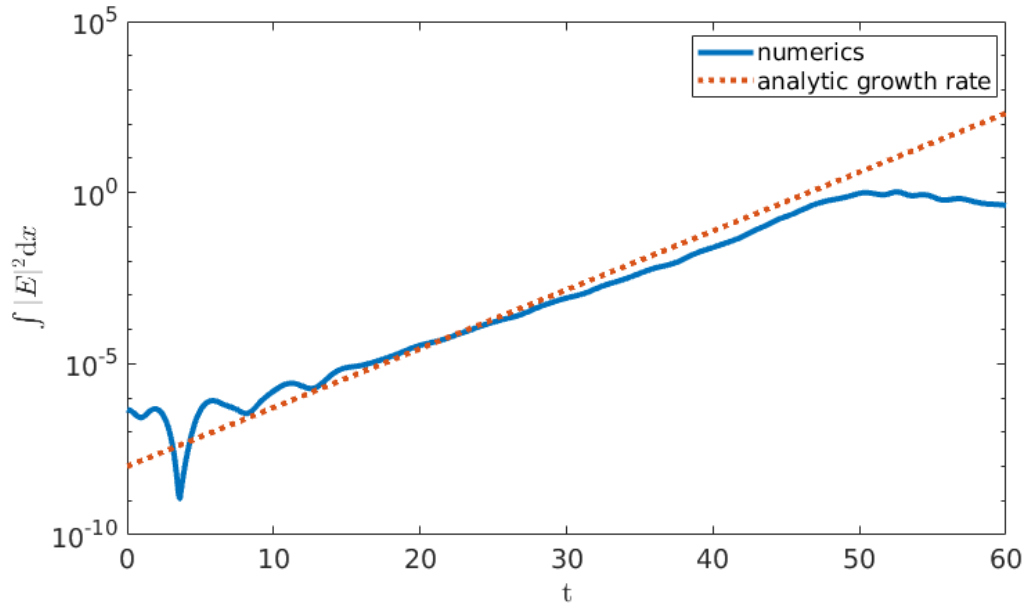


Figure 4.9.: Bump-on-tail instability test with $k = 0.3$, $\epsilon = 0.001$, $v_b = 4.5$, $n_b = 0.1$ and $N_k = 10^5$.

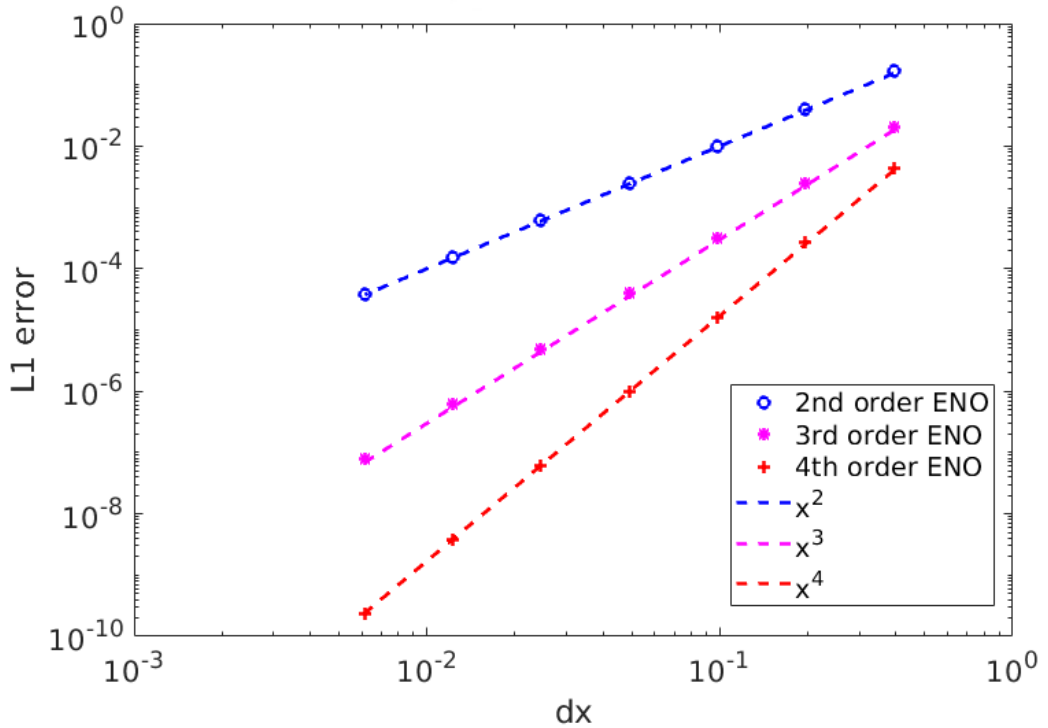


Figure 4.10.: ENO reconstruction according to (3.27) of the function $Z(x) = \sin(x)$ with different space discretizations Δx . The order of the convergence is indicated by the dashed lines.

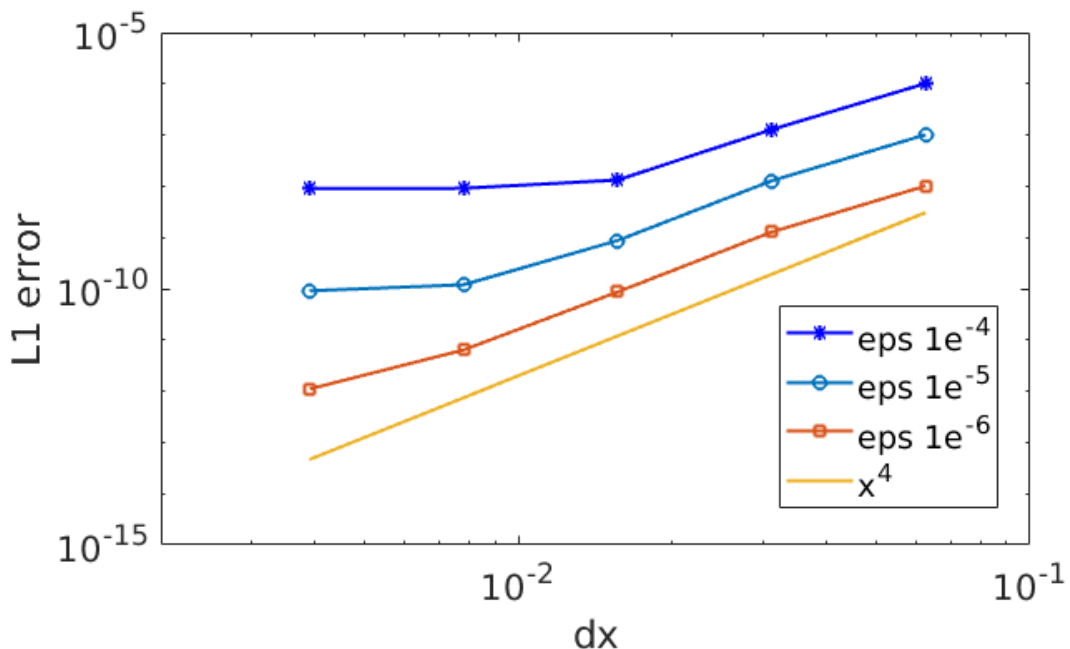


Figure 4.11.: Comparison of the ENO4-RK4 solution to the exact (linearized) solution of the Euler equations with initial conditions (4.6), for different Δx and ϵ .

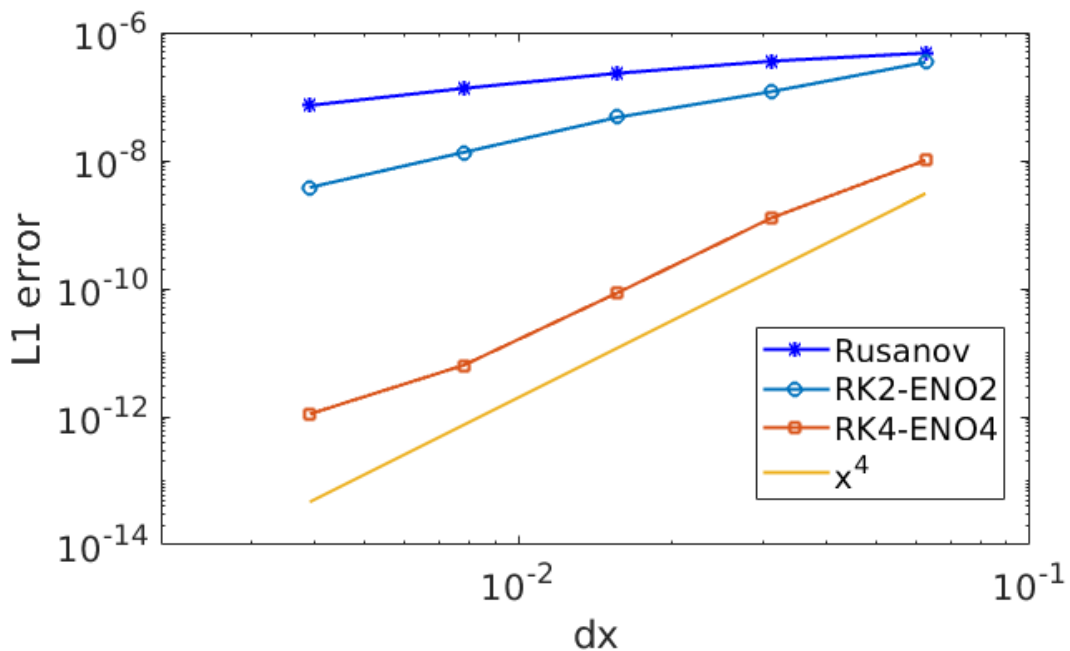


Figure 4.12.: Convergence test of ENO-RK schemes of different order for the Euler equations, with initial conditions (4.6).

4. Simulation Results

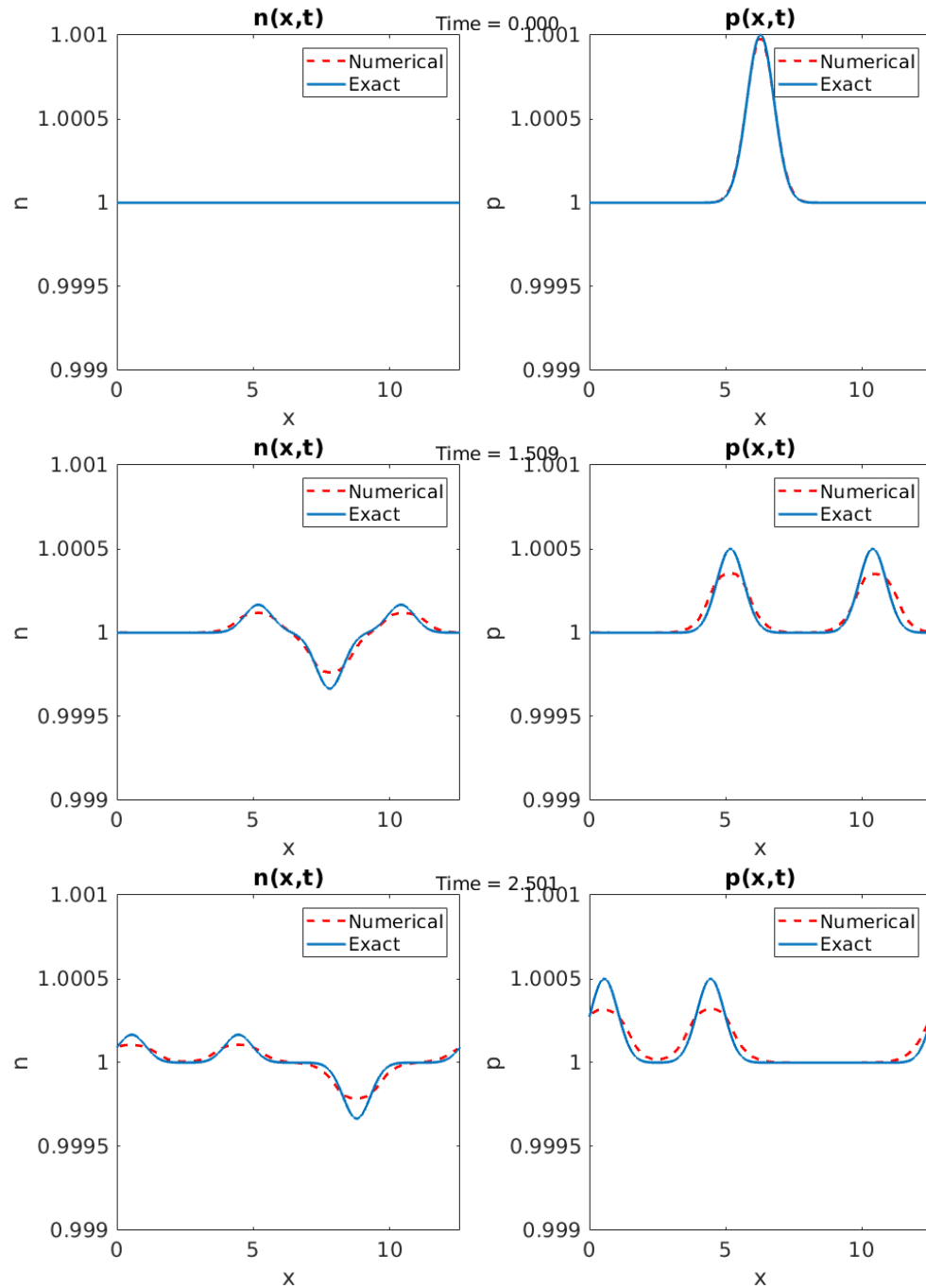


Figure 4.13.: Evolution of n and p with respect to time for $N_x = 64$ and with initial conditions (4.7). The scheme used is the ENO 4th order reconstruction with RK4 time discretization.

4. Simulation Results

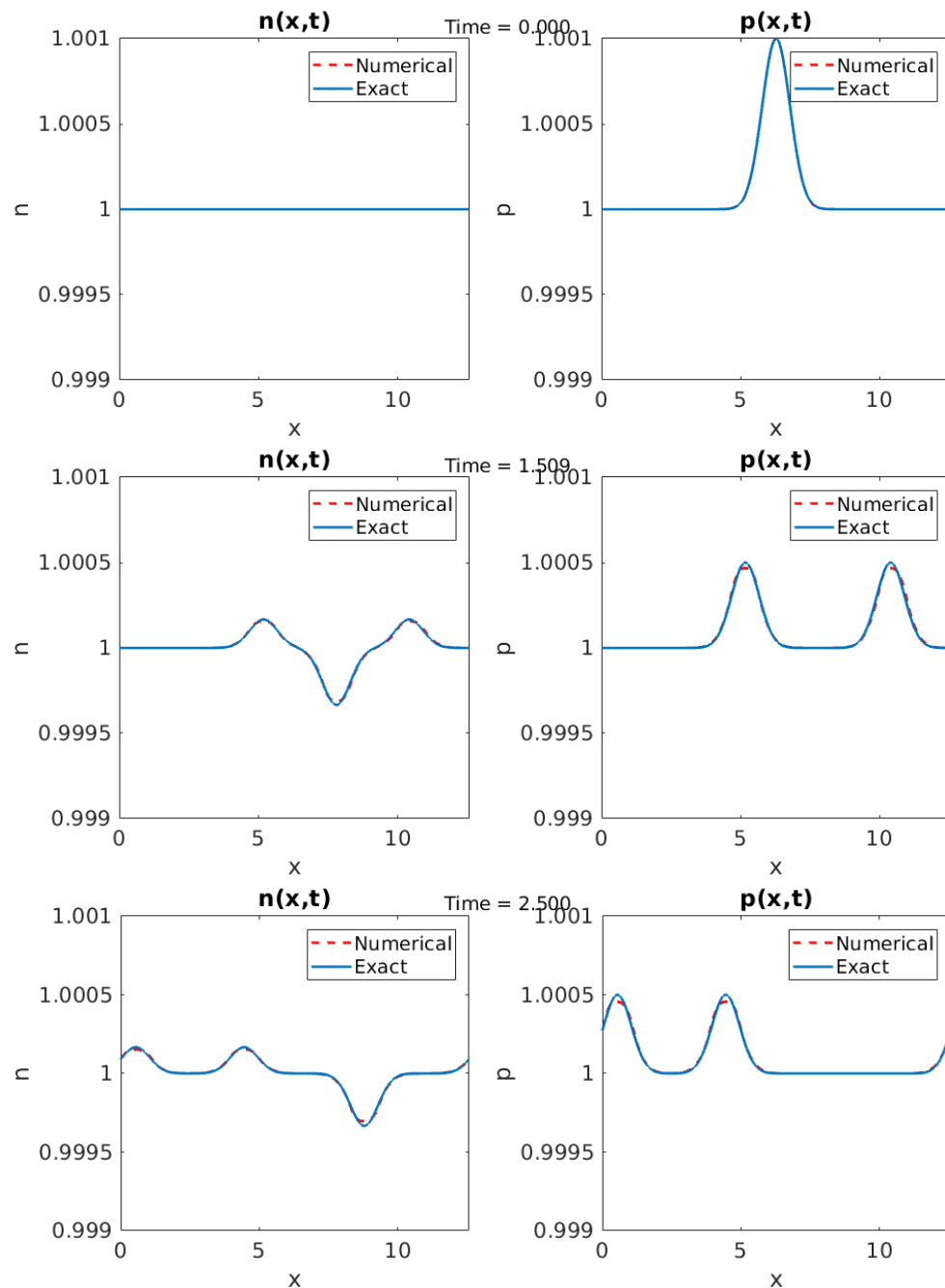


Figure 4.14.: Evolution of n and p with respect to time for $N_x = 256$ and with initial conditions (4.7). The scheme used is the ENO 4th order reconstruction with RK4 time discretization

4. Simulation Results

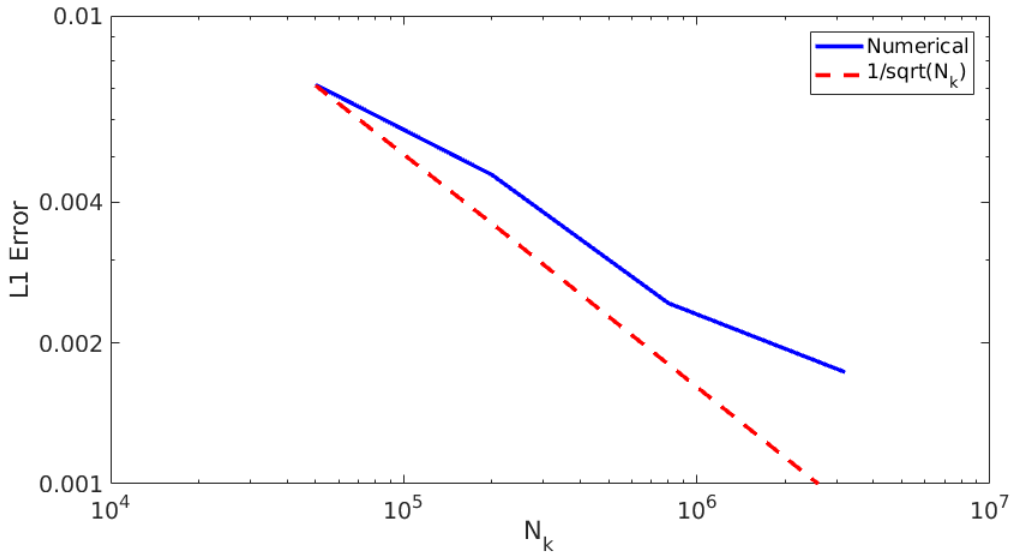


Figure 4.15.: Convergence plot of the L^1 -error in fluid density when compared with the analytical density obtained from (2.16). The PIC density is used for the electric field computation. The dashed line indicates the expected MC convergence rate.

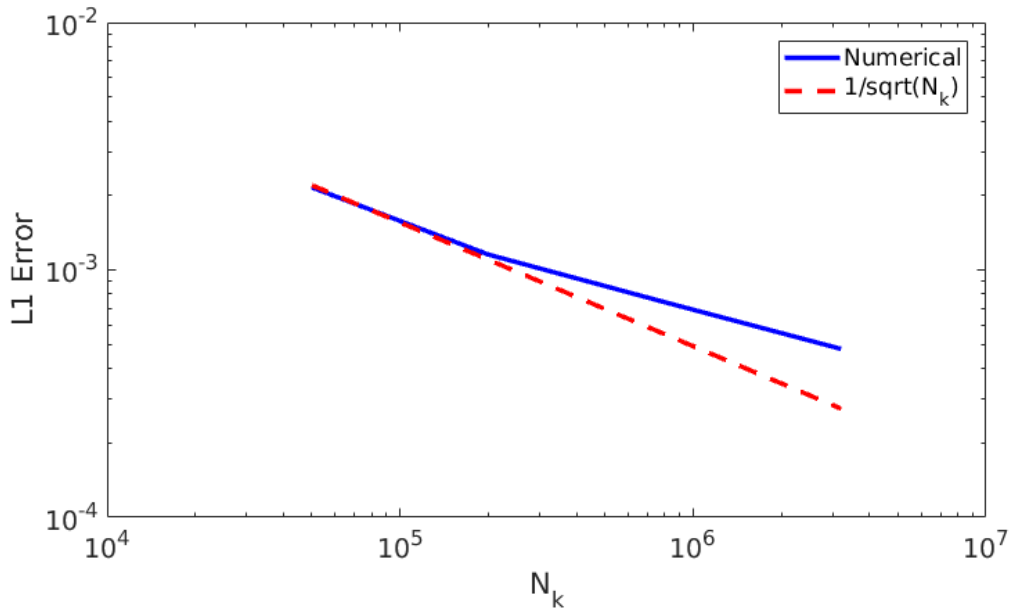


Figure 4.16.: Convergence plot of the L^1 -error in fluid density when compared with the analytical density obtained from (2.16). The fluid density is used for the electric field computation. The dashed line indicates the expected MC convergence rate.

4. Simulation Results

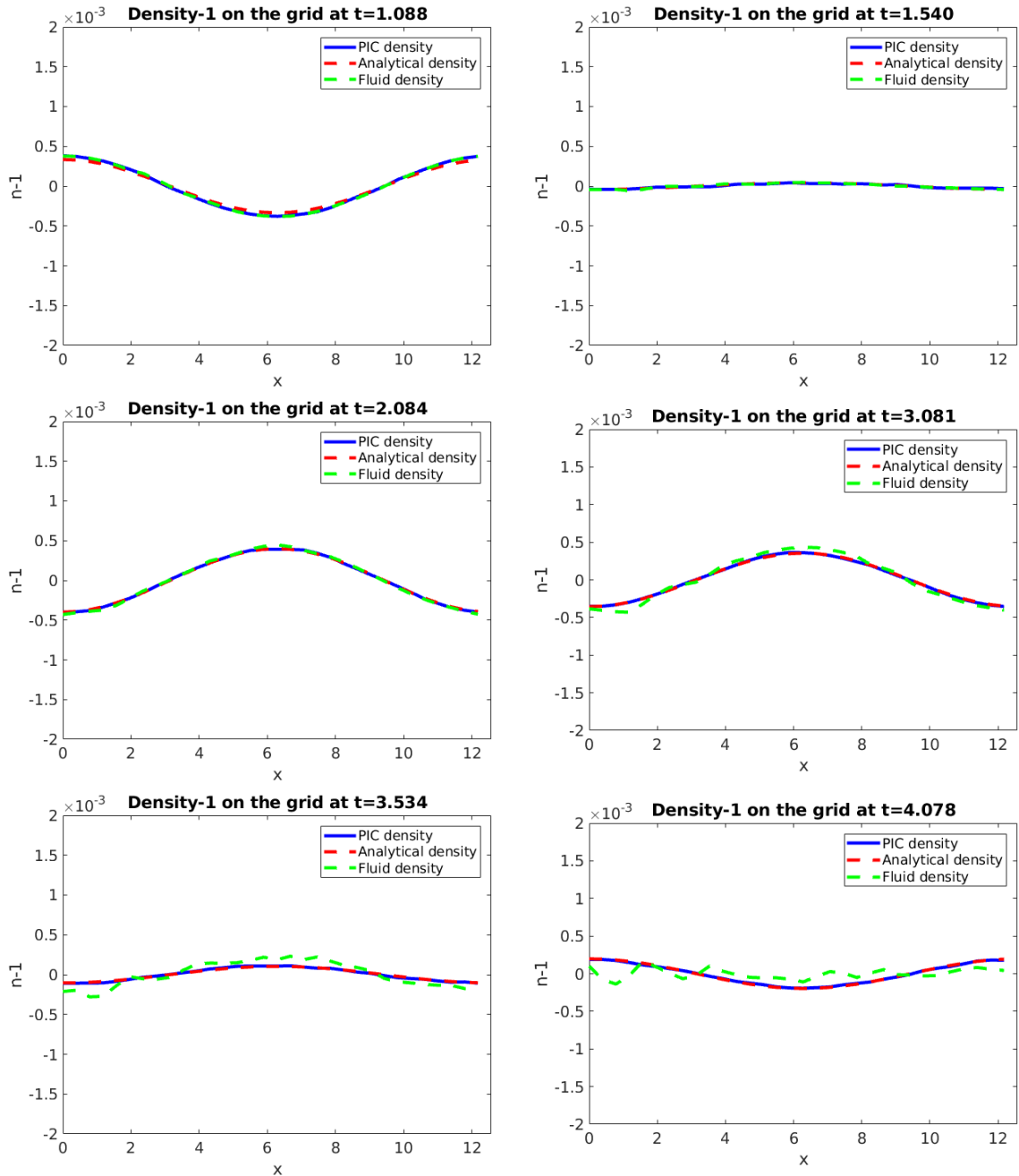


Figure 4.17.: Evolution of PIC, fluid and analytical density, when PIC density is used for electric field calculation, with $N_k = 8 \times 10^5$

4. Simulation Results

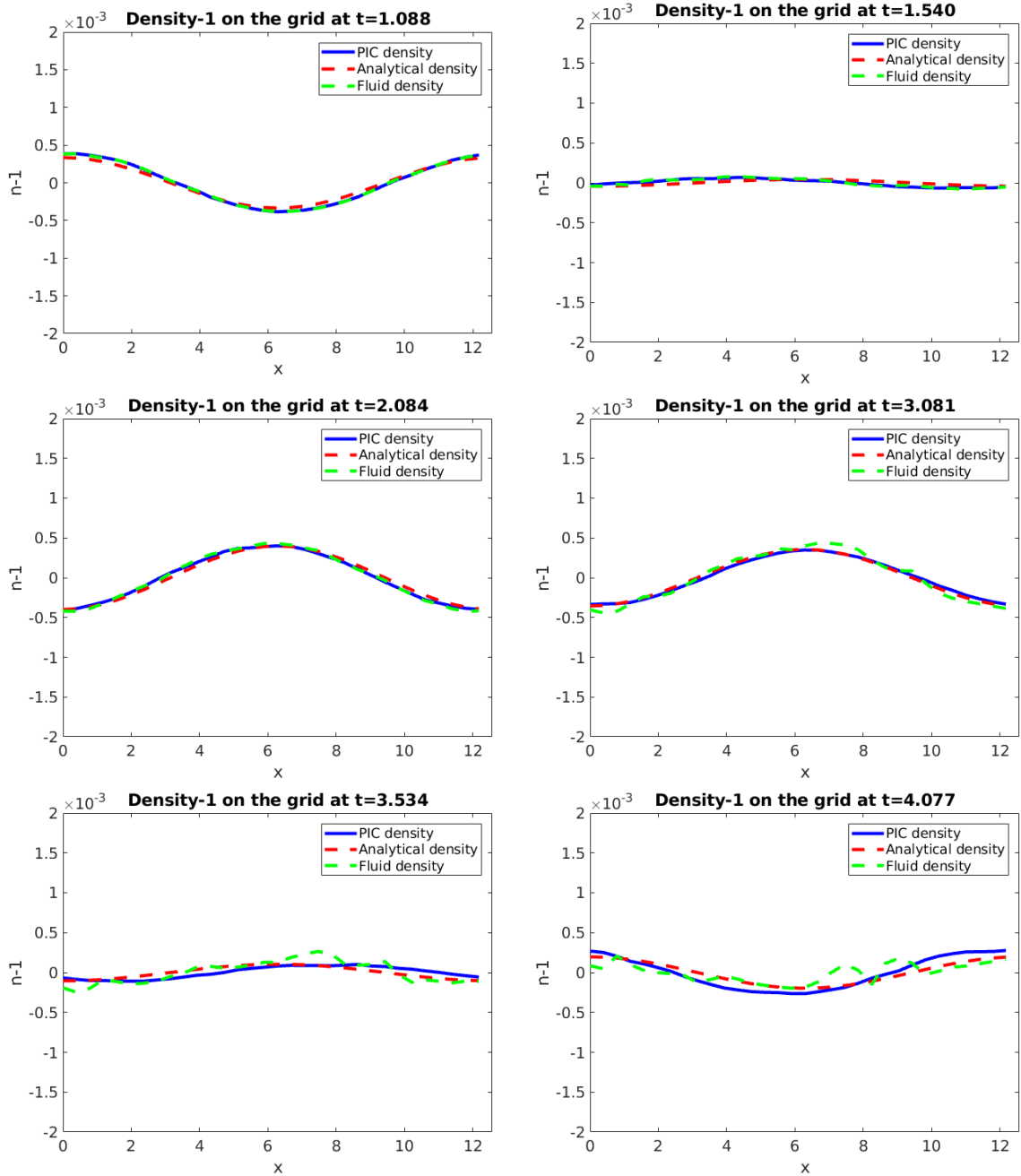


Figure 4.18.: Evolution of PIC, fluid and analytical density, when the fluid density is used electric field calculation, with $N_k = 8 \times 10^5$

5. Conclusion

The topic of the thesis was the implementation of a kinetic-fluid hybrid code for the one-dimensional Vlasov-Poisson system. The PIC and fluid solvers were implemented and tested individually. The observed convergence rates and the verification tests show that both solvers and the underlying mathematical models were implemented correctly. In the next stage, in order to device a hybrid scheme, we coupled these solves through the *heat flux* term, which is calculated by the Monte-Carlo method. The idea is to advance the fluid variables with a heat flux that is accurate enough so as to yield the correct fluid quantities from the finite volume solver even when f departs from equilibrium. First tests in this direction have been performed in the last section of this thesis. Even though we are not yet able to control the variance of the MC q computation in a satisfactory manner, the obtained MC convergence rate of $\frac{1}{\sqrt{N_k}}$ encourages further studies in this direction.

Bibliography

- [1] Charles K Birdsall and A Bruce Langdon. *Plasma physics via computer simulation*. CRC press, 2004.
- [2] Pierre Degond, Giacomo Dimarco, and Luc Mieussens. A moving interface method for dynamic kinetic–fluid coupling. *Journal of Computational Physics*, 227(2):1176–1208, 2007.
- [3] J F Bourgat, P Le Tallec, Benoit Perthame, and Y Qiu. Coupling Boltzmann and Euler equations without overlapping. 157, 01 1994.
- [4] Richard D Hazeltine and James D Meiss. *Plasma confinement*. Courier Corporation, 2003.
- [5] T. M. M. Homolle and N. G. Hadjiconstantinou. Low-variance deviational simulation Monte Carlo. *Physics of Fluids*, 19(4):041701–041701, April 2007.
- [6] H. Hora. Nicholson D. R., Introduction to Plasma Theory, John Wiley & Sons, New York, 1983, XII, 292 pp. *Laser and Particle Beams*, 2(1):127–127, 1984.
- [7] John A. Krommes. Fundamental statistical descriptions of plasma turbulence in magnetic fields. *Physics Reports*, 360(1):1–352, 2002.
- [8] Randall J. LeVeque. *Finite Volume Methods for Hyperbolic Problems*. Cambridge Texts in Applied Mathematics. Cambridge University Press, 2002.
- [9] Chi-Wang Shu. *Essentially non-oscillatory and weighted essentially non-oscillatory schemes for hyperbolic conservation laws*, pages 325–432. Springer Berlin Heidelberg, Berlin, Heidelberg, 1998.